LLE Review

Quarterly Report

October–December 1984

UR
LLE

LLE Review

Quarterly Report

Editor: H. Kim
(716) 275-5850

October–December 1984

IN BRIEF

This volume of the LLE Review contains articles on upgrade of the GDL system, theoretical advances in the laser fusion effort, improved target fabrication capabilities, x-ray laser research, developments in the picosecond optics research of the LLE advanced technology program, and on the National Laser Users Facility activities for October–December 1984.

The following are some highlights of the work described in this issue:

- The second group of six OMEGA beams has been converted from an IR (1054-nm) to a UV (351-nm) output, and output energy of the 12 frequency-tripled beams has reached 1056 J.

- GDL has been upgraded with four 25-cm-diameter active mirror amplifiers to generate in excess of 300 J at 1054 nm in 1-ns pulses.

- Six Brewster-angle linear polarizers in GDL have been replaced with liquid crystal polarizers. The liquid crystal polarizers eliminate some disadvantages associated with the Brewster-angle polarizers and provide effective optical isolation and back reflection protection.

- A simplified electron thermal transport theory has been developed. This model is self-consistent and gives the heat flux as a nonlocal convolution of given density and temperature profiles.

- During the sputter coating process of pusher layer deposition, pulsed nitrogen gas has been injected. As a result, columnar growth of the

film formation has been completely suppressed, and a very smooth surface finish has been obtained.

- Two novel approaches to the development of a linear uniform medium suitable for x-ray gain conditions have been investigated. This initial investigation has provided some interesting data from which future studies can optimize the production of linear plasma.

- A technique has been demonstrated which can characterize very high-speed semiconductor devices. The method is capable of characterizing the response of microstructures with a temporal resolution of a fraction of a picosecond.

- High-repetition-rate amplification of ultrashort optical pulses to the microjoule level has been achieved using a recently developed kHz Nd:YAG regenerative amplifier and a synchronously pumped CPM dye laser.

CONTENTS

Thomas Boehly, a graduate student in mechanical engineering, prepares plasma and light calorimeters for laser-plasma experiments in the GDL target chamber. These experiments measure the hydrodynamic efficiency of planar targets.

Section 1
LASER SYSTEM REPORT

1.A GDL Facility Report

During the first quarter of FY85, the upgrade of the glass development laser (GDL) facility was started and completed. This includes successful installation and activation of active mirror amplifiers. Limited damage test experiments and target interaction experiments in the Beta target chamber were also conducted. A detailed description of the active mirror amplifiers is given in Section 1.C.

The frequency conversion cells were assembled and will be installed soon. A multi-wavelength energy-sensing system (MESS) similar to the OMEGA system has been designed, and appropriate software for acquisition and reduction of beamline energy data has been implemented. This will all be installed in the GDL system during the next shutdown period, after 1 January 1985.

During this quarter, the GDL facility was used as a single-beam IR laser with substantially more energy output.

A summary of GDL operations during this quarter follows:

Interaction Shots	73
Damage-Testing Shots	134
Alignment, Test Shots	163
TOTAL	370

1.B   OMEGA Facility Report

OMEGA operations for this quarter consisted of work in the following areas: (a) completion of the wavelength conversion of the second group of six OMEGA beams from an IR (1054-nm) to a UV (351-nm) output; (b) activation of the 12 frequency-tripled beams; (c) target irradiation experiments with these 12 beams; and (d) cessation of laser operation for the final frequency conversion of the remaining 12 beams.

During October the components were assembled and installed for the conversion, and the first successful 12-beam target shot was achieved. The 12-beam system was fully characterized, and included a full scan of the beam waists of the focused beams, near-field photographs of all 12 beams, and a fine tuning of all conversion cells. Modifications to the polarization in the driver improved its output energy, allowing beamline energy to exceed 1 kJ; the highest energy achieved was 1056 J.

During this period, several new diagnostic instruments were activated. In particular, the radiation chemistry system has been successfully implemented, activated, and tested. The initial results were good. During the x-ray laser experiments, the activation of the shuttle target positioner allowed targets to be inserted into the target chamber without the need for a vacuum break. At the beginning of the x-ray laser campaign, cylindrical correction lenses were installed into the focus lens mounts, allowing line-focused beams to be put onto targets. Alignment techniques were devised to allow these line beams to be targeted in different configurations on both planar and cylindrical targets.

Laser operations ceased in November in order to enable frequency conversion of the last 12 beams of OMEGA. Prior to the cessation, the MESS photodiodes were precalibrated. In the calibration, the active 12 beams were used as energy sources and the calibrated diodes in the integrating spheres as the references. By this precalibration, much time can be saved during the 24-beam activation, obviating the calibration of the new photodiodes. During the last part of November and the early part of December, structures for the last 12 beams were placed and alignment of the beamlines was completed. Other activities for the 24-beam conversion during this quarter included: (a) construction, sizing, and alignment of spatial filters; (b) modification to the driver line, allowing higher output energy; (c) an attempt to eliminate the spark-gap firing of Pockels cells 4 and 5; and (d) an upgrade of the beam diagnostics package in the driver. As a result, completion of the 24-beam OMEGA UV-laser system is on schedule.

A summary of OMEGA operations during this quarter follows:

Software Test Shots	21
Driver Test Shots	75
Beamline Test Shots	50
Target Shots	88
TOTAL	234

ACKNOWLEDGMENT

1.C GDL Facility Upgrade

LLE has been engaged in the development of various Nd:glass amplifiers over the past ten years.[1,2] Development of the active mirror amplifier did not progress significantly until midway in this ten-year period, when in-house thin-film design and fabrication were made available. Concurrent with major advancements in hardware development, this thin-film capability contributed to the successful implementation of a four-unit, 17-cm clear aperture active mirror system.[3] Soon afterwards, preliminary studies of a 25-cm active mirror prototype revealed several unanticipated problems with the mounting, sealing, and coolant flow designs that were not encountered on the smaller version of the active mirror amplifier.

Recent progress in hardware development involving a new active mirror mounting and sealing design has resulted in the successful upgrade of GDL with four 25-cm-diameter active mirror amplifiers. The key features of the active mirror design are illustrated in Fig. 21.1. A 3-cm-thick LHG-8 slab is situated within an annulus of parasitic-inhibiting glass beads and is held firm with a conventional three-point mounting scheme. A bead of silicon-based sealant attaches the edge of the slab to the mirror holder, thus forming the front half of a liquid tight seal. This technique reduces the problem of pressure-induced slab distortions, previously caused by O-ring seals, without compromising the reliability of the liquid seal. The cooling system is also designed to minimize slab distortions. A mixture of ethylene glycol and water is pumped from an external reservoir to the top of the channel between the blast shield and the rear surface of the slab; at the same time, the coolant leaves the bottom of the channel to bring the mirror and the reservoir in gravitational equilibrium. This flow provides adequate cooling without significant slab distortion.

Coolant Entry

Coolant Area
(edges and back)

Glass Beads

Sealant

Reflective
Coating

Input Beam

Anti-Reflection
Coating

Blast Shield

Active Mirror
Slab

Reflector

Amplified
Output
Beam

Water-Jacketed
Flashlamps

Swivel Pad

Tabs

Side Angle

O-Ring Seal

To Coolant
Reservoir

Face Angle
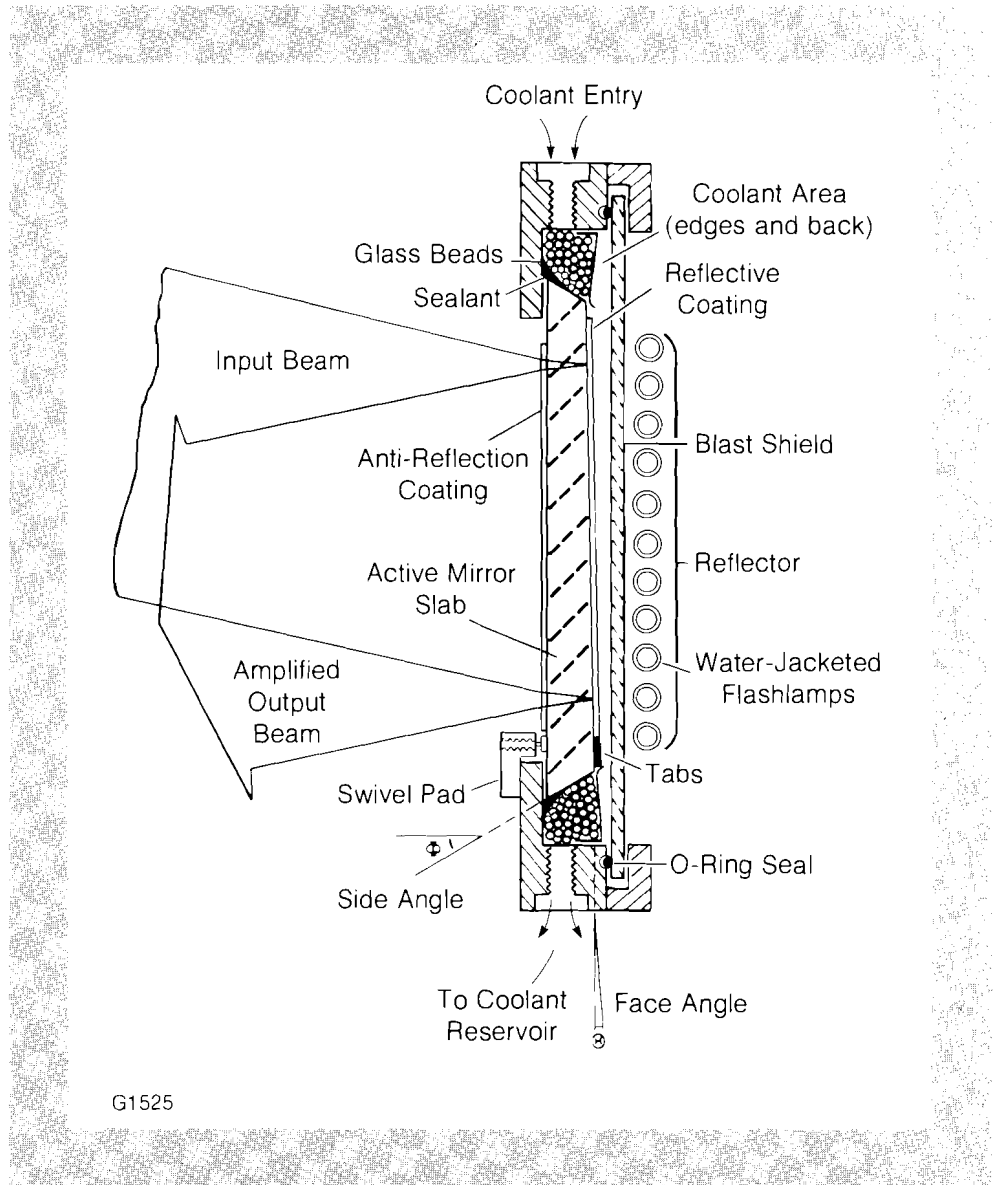
G1525

Fig. 21.1
Key features of the active mirror design. The slab is pumped by flash-lamp light entering through the surface facing the blast shield. This surface is coated to transmit useful pump bands and reflects the laser beam to be amplified. The incident laser beam enters through the front of the slab, reflects from the rear surface and exits, completing an energy-extraction path that is twice the slab thickness.

The optical pump module contains an array of water-jacketed xenon flash lamps which are closely coupled to the mirror holder. The flash lamps vary in length in order to form three pulse-forming networks of equal, total discharge length. The active mirror slab is pumped by the flash-lamp light entering through the surface facing the array. This surface is coated to allow useful pump bands to be transmitted into the slab while reflecting the laser light to be amplified. The laser beam thus makes a double pass through the slab and completes an energy extraction path that is twice the slab thickness.

During the active mirror upgrade to GDL, many improvements were made from both an operational and an experimental point of view. The laser system is schematically illustrated in Fig. 21.2. The Faraday rotator is repositioned between the second 64-mm and the 90-mm rod amplifiers to provide optical isolation between two major gain sections of the laser system. Liquid crystal circular polarizers are located throughout the

4

Key:
- F.R. — Faraday rotator
- H.A. — hard aperture
- ▰◗◖▰ — spatial filter
- [▬] — rod amplifier
- ▬ — liquid-crystal circular polarizer
- ═ — active mirror amplifier
- — · — · — λ/4 retardation plate
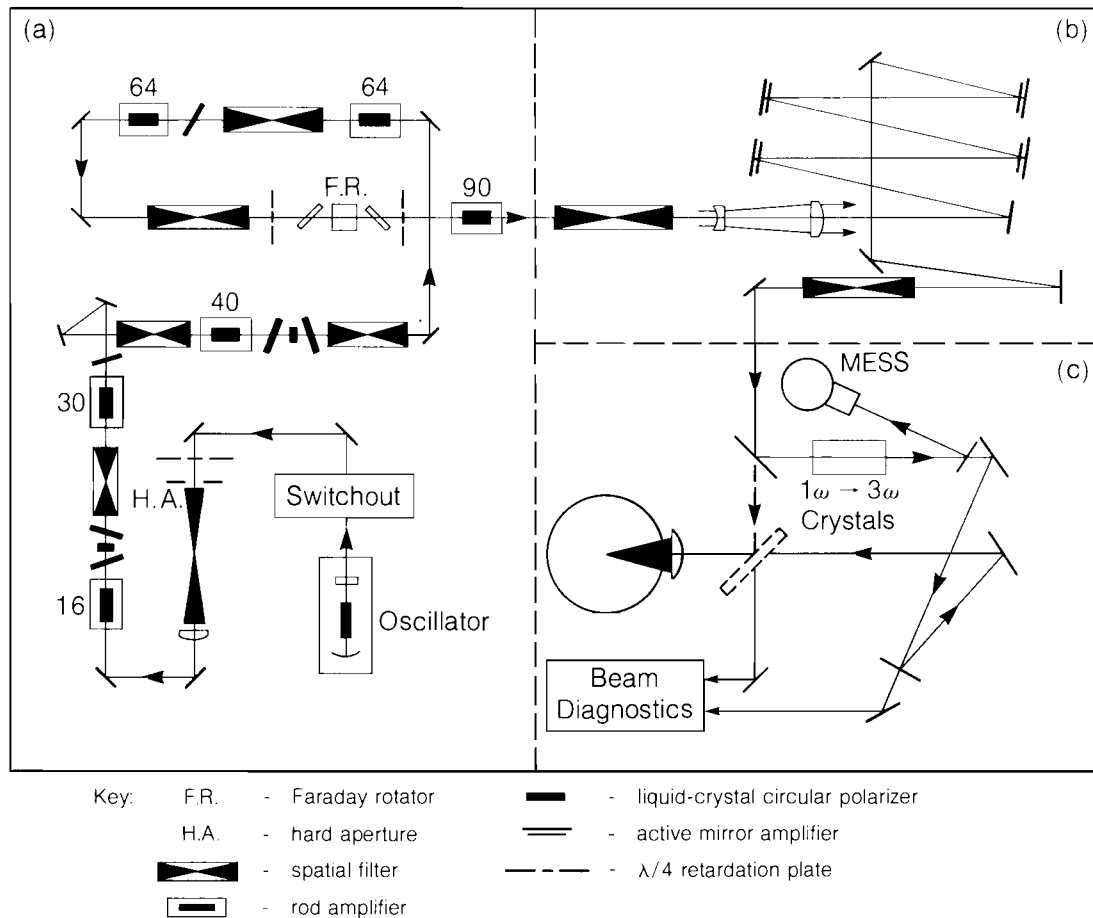
G1522

Fig. 21.2
The GDL system (a) characterized by six amplification stages that follow an active/ passive mode-locked oscillator, operating at 1054 nm in 1-ns pulses. The output is upcollimated to 20-cm diameter and directed to a series of four active mirror amplifiers (b). The amplified IR beam either propagates directly into the Beta target chamber for 1-μm experiments or is frequency converted for short-wavelength experiments (c).

driver line to allow for the propagation of circularly polarized light through each of the rod amplifiers. The main advantages of this polarization scheme are described in Section 1.D.

The output of the previous GDL system is upcollimated to a beam diameter of 20 cm and directed into a series of four active mirror amplifiers. Figure 21.2(b) schematically illustrates the single-pass configuration, where the incident laser beam reflects only once from each of the active mirrors. Alternatively, in the double-pass option,[4] a retro-reflecting mirror is positioned after the fourth active mirror in order to return the laser beam through the same series of active mirrors. In this scheme, a thin-film polarizer and mica quarter-wave plate are employed to separate the forward and return beams. In either configuration, the laser beam leaving the active mirror amplifiers is spatially filtered and injected into the Beta irradiation facility. Then the IR beam either propagates directly into the target chamber for IR interaction experiments or is frequency converted for short-wavelength interaction experiments [see Fig. 21.2(c)].

The active mirror single-pass and double-pass performances at 1 ns have been studied in detail. The overall active mirror gain, shown in Fig. 21.3, represents the case where only one of the four single-passed slabs has a front face coating. Although the total output was thus reduced by multiple Fresnel reflection losses, the active mirror amplifiers have produced in excess of 300 J at 1054 nm in 1-ns pulses. Unfortunately, the double-pass performance is not only reduced by the multiple Fresnel losses but also suffers from stored energy depletion due to the numerous Fresnel-reflection-generated beams which are separated slowly from the main laser beam. Additionally, a 27% loss is suffered from the polarization components required to separate the forward and returning laser beams. However, it is expected that the double-pass gain will be significantly increased once the front surface of each of the four active mirrors is AR coated in the near future.

G1523
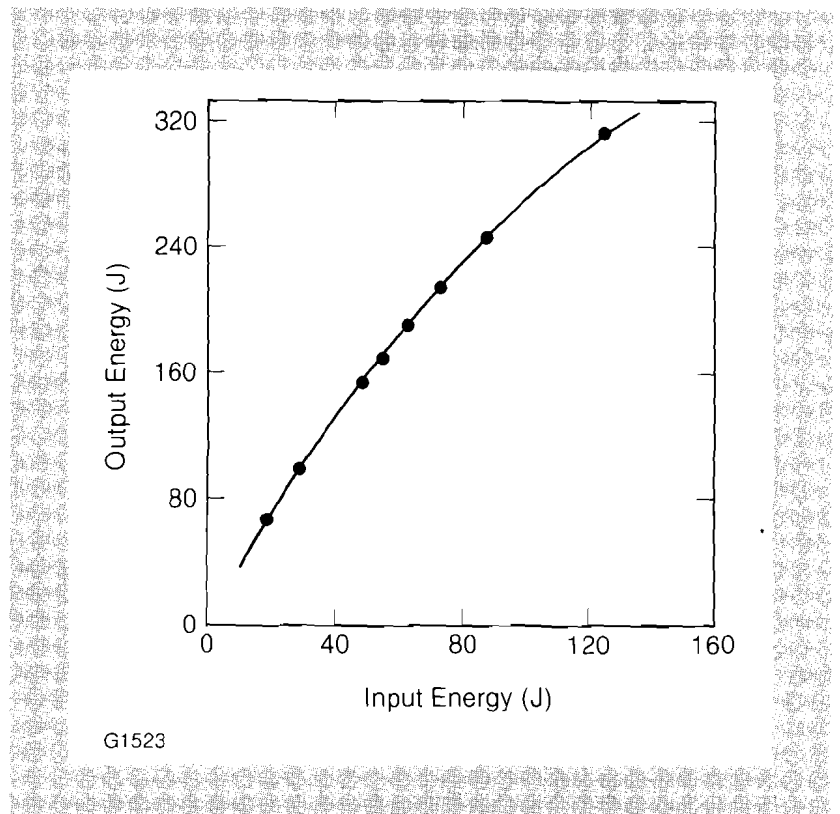
Fig. 21.3
One-nanosecond performance for a four-unit, single-passed active mirror booster to GDL. One of the four 2.5%-doped LHG-8 active mirrors was AR-coated on its front surface.

The near-field distribution, measured after the final spatial filter, indicates that the new amplification chain does not adversely affect the energy distribution. Preliminary phase measurements, using lateral shearing interferometry, have indicated that the collimating lens at the input to the active mirror sufficiently compensates the positive defocus that is inherent in slab amplifiers cooled through the rear surface.

Several experiments were conducted to evaluate beam alignment and focusing accuracy as well as beam focusability. X-ray pinhole photography has shown that the energy distribution has a triangular envelope for focusing conditions ahead of best focus. Equivalent-target-plane photography concurs but yields a more accurate picture of the energy

distribution within this envelope. The triangular shape originates from the cumulative wave front distortion introduced to each unit by the three-point mounting of the slab. Preliminary cw tests indicate that most of this distortion can be removed by properly adjusting the mounts after installation (see Fig. 21.4). Furthermore, rotation of two active mirror holders is expected to change this distribution into a less-pronounced hexagonal envelope. Although our effort to obtain uniform, round intensity distributions at the target plane continues, the beam envelope control inherent in the active mirror mounting design will be used to study alternate methods of intensity and phase correction. These are currently under investigation in the LLE uniformity program.

(a) ◄——4 mm——►   (b) ◄——4 mm——►
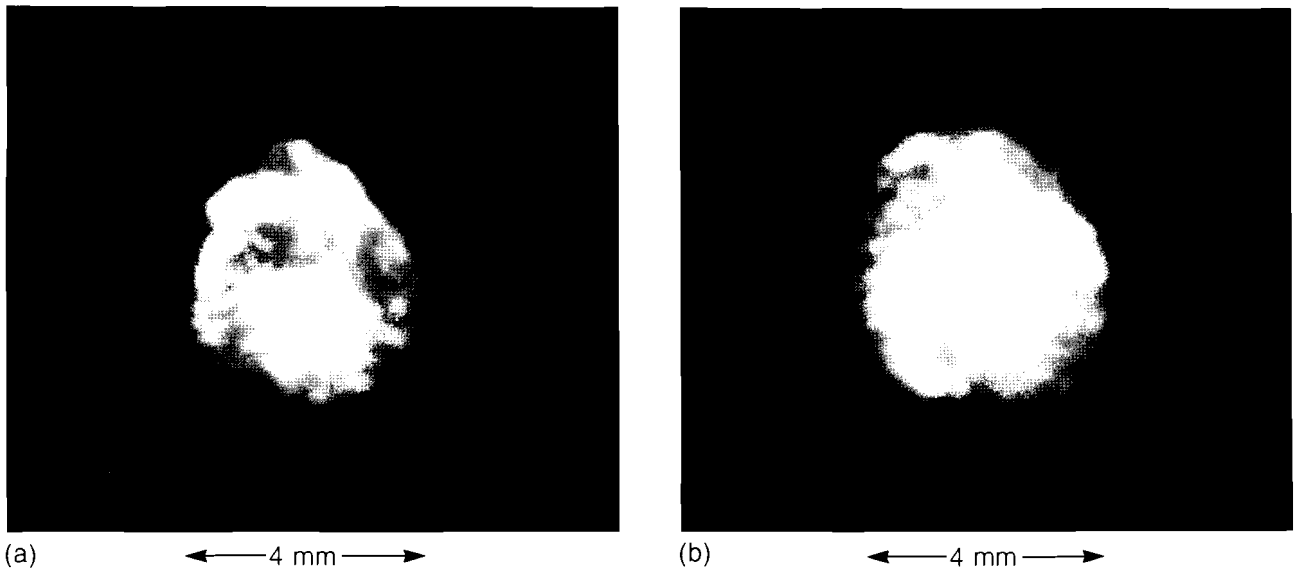
G1527

Fig. 21.4
A quasi-far-field intensity distribution from a YAG alignment laser in GDL shows the triangular envelope resulting from the cumulative wave-front deformation of four active mirrors (a). Active control of this distortion, obtained from proper adjustment of the mounts, is illustrated with the removal of most of the distortion (b).

In summary GDL has been upgraded with four 25-cm-diameter active mirror amplifiers to generate in excess of 300 J at 1054 nm in 1-ns pulses. Recent progress in hardware development involving a new active mirror mounting and sealing design has resulted in low slab distortion and increased reliability. Active mirror beam characterization has provided useful information that is the basis for further active mirror development. Concurrent with this upgrade, liquid crystal circular polarizers were tested and installed in the GDL amplifier chain.

ACKNOWLEDGMENT

REFERENCES

1. J. Hoose and J. Soures, presented at the Conference on Laser Engineering and Applications, paper 4.1 (1975).

2. Laboratory for Laser Energetics Annual Report 1, 10–18 (1977).

3. J. A. Abate, L. Lund, D. Brown, S. Jacobs, S. Refermat, J. Kelly, M. Gavin, J. Waldbillig, and O. Lewis, *Appl. Opt.* **20**, 351 (1981).

4. D. C. Brown, J. A. Abate, L. Lund, and J. Waldbillig, *Appl. Opt.* **20**, 1588 (1981).

1.D Retrofit of the GDL System with Liquid Crystal Polarizers

Brewster-angle linear polarizers composed of alternating high- and low-index, thin-film layers that have been deposited on glass substrates have been utilized in the GDL system at LLE since it was first constructed. Produced by standard e-gun deposition technology in apertures ranging from 2 cm to 20 cm, these optical elements routinely achieve polarization levels of 200 to 500:1 at 1054 nm with good laser damage resistance. They are essential to the operation of electro-optic switching devices such as Pockels cells. Three disadvantages to Brewster-angle polarizers include environmental instability, tendency to displace the laser system beamline, and physical space requirements.

We have recently replaced six Brewster-angle linear polarizers in GDL with liquid crystal (LC) polarizers, varying in clear aperture from 38 mm to 100 mm.[1] Figure 21.5 shows the locations of the liquid crystal cells

Fig. 21.5
GDL Nd:glass laser system with liquid crystal polarizers. The six circular polarizers vary in clear aperture from 38 mm to 100 mm and permit the propagation of circularly polarized laser radiation through most of the beamline.
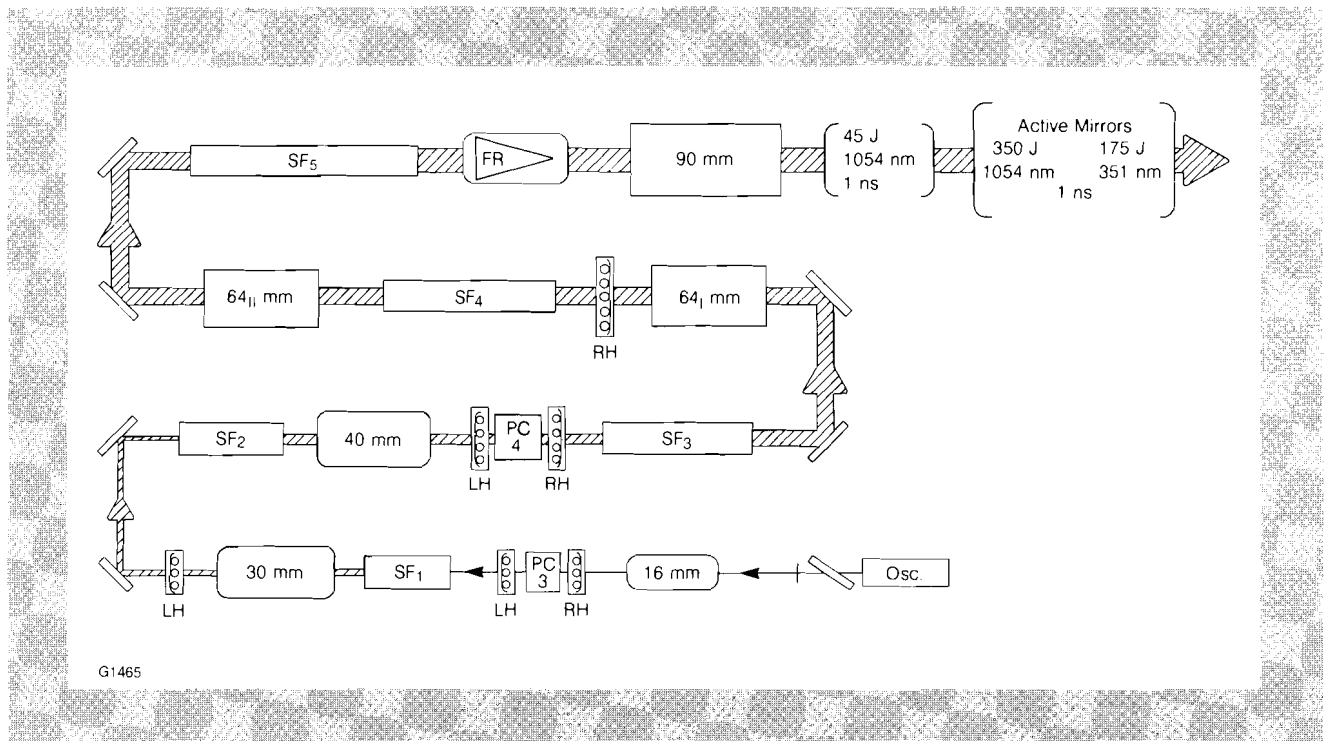
in the system, which has been reconfigured to drive active mirror amplifiers. Liquid crystal polarizers have none of the disadvantages associated with Brewster-angle polarizers and offer additional features not available with any other polarizer technology. Figure 21.6 shows how, in addition to serving as polarization elements for electro-optic switches, liquid crystal cells can provide optical isolation or back reflection protection. This versatility has permitted us to incorporate the following changes in reconfiguring the GDL system:

1. propagation of circularly polarized laser radiation through the entire front end, minimizing stress birefringence induced by the laser rods;

2. relocation of the Faraday rotator toward the output end of the system, providing for better protection against system back reflection;

3. reduced concern with back reflected ghosts, due to the isolation properties of the LC polarizers;

4. improved throttle adjustment at the oscillator input to the beamline with the use of circular polarization; and

5. ease of installation and alignment.

In this article we describe the in-house design, fabrication, installation, and testing of liquid crystal polarizers on GDL.

Fig. 21.6
Dual function of liquid crystal polarizers. Left-handed (LH) and right-handed (RH) circular polarizer elements may be fabricated and installed to perform traditional polarizer/analyzer functions in electro-optic switch-out devices. In addition, they act as optical isolators to prevent beamline component damage due to specular back reflections from fusion targets or ghosts.

The uses of liquid crystals for high-power laser applications have been discussed in the literature[2,3,4] and in previous volumes of LLE Review. In Volume 5 we described the property of selective reflection in cholesteric liquid crystal cells and the possibility of their use as optical isolators. Volume 6 contained research results for nematic liquid crystals as wave plates, and in Volume 15 we presented the concept of liquid

crystal, laser-blocking notch filters. Briefly reviewed, selective reflection occurs in organic liquid crystal compounds when left-handed (LH) or right-handed (RH) chiral additives are mixed into base nematics so that a helical twist structure results. As Fig. 21.7 shows, if the pitch P, characteristic of this twisted structure, satisfies the equation

$$\lambda_o = \bar{n}P \tag{1}$$

Fig. 21.7
Selective reflection and Bragg-like interference. The chiral structure of liquid crystals will selectively reflect incident laser radiation if the laser's sense of circular polarization and wavelength equal the product of helical pitch times average liquid refractive index. Otherwise, no interaction occurs.

where $\bar{n}$ is the average refractive index of the liquid, then incident laser radiation at wavelength λ_o experiences Bragg-like interference and diffuse reflection for that circularly polarized component that rotates in the same sense as the helical structure. By using two cells in tandem, each filled with a fluid layer whose pitch and refractive index are tuned by compound blending to satisfy Eq. (1) but with *opposite* chirality, laser radiation of any arbitrary polarization state can be polarized and rejected by the cells. They act as a pair of crossed, circular polarizers at λ_o.

Molecular planes order
in RH helix

3Å

Unpolarized
Incident

P

Case A: $\lambda \neq \lambda_o$
- No interaction
- Complete transmission

RH helix

LH

RH

Case B: $\boxed{\lambda_o = \bar{n}P}$
- Strong interaction for one chirality
  - selective (diffuse) reflection
- No interaction for opposite chirality
  - complete transmission

λ, laser wavelength $\bar{n}$, average refractive index for liquid crystal
λ_o, wavelength of selective reflection   P, pitch of structure

G1469

Figure 21.8 shows spectral absorptance in unpolarized light for LH and RH cells tuned to 1064 nm. Scanned separately, each fluid exhibits a selective reflection peak with few other features between 300 nm and 2000 nm. When scanned together, the composite exhibits strong extinction near 1064 nm.

Cell fabrication begins with selection of the compound. Table 21.I lists the pure, base nematics that we have selected from commercial sources. They represent eutectic mixtures of long, rodlike molecules whose terminal and bridging groups are chosen to optimize properties such as melting and clearing points, viscosity, birefringence, optical

$\lambda_p = 1064$ nm

Crossed Pair

LH — — RH

Single Elements

Optical Density

Wavelength (nm)

G1470

Fig. 21.8
Spectral transmission through liquid crystal polarizers. Single LH and RH element scans indicate that, apart from regions of increased optical density due to selective reflection, the spectral transmission of liquid crystal polarizers is featureless. Crossed polarizers exhibit blocking extinction at any desired wavelength, which is determined by tuning liquid crystal pitch with composition mixing.
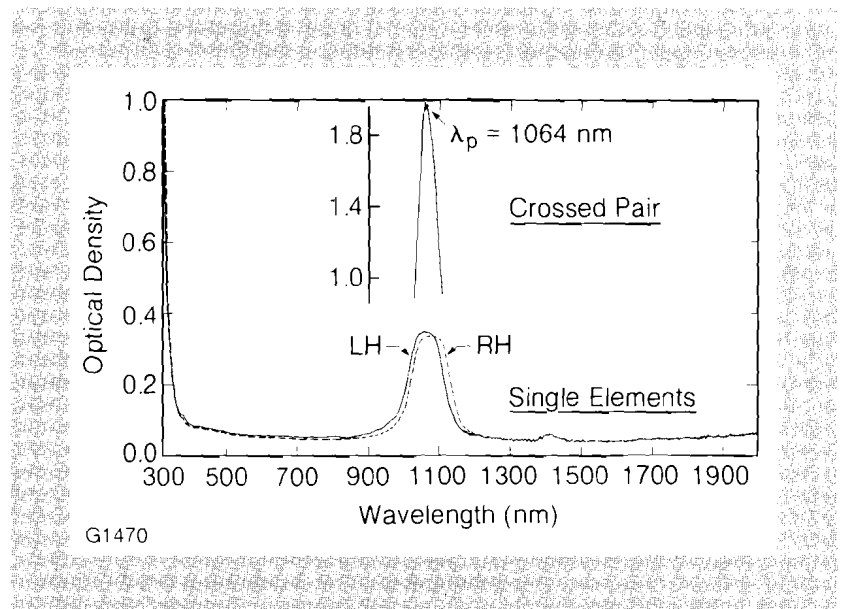
transmittance, and environmental stability. The base nematics are all liquids at room temperature. The LH and RH chiral additives listed in Table 21.I may be solids (wax or powder) or liquids. The quantity of additive required for pitch tuning depends upon the intrinsic pitch of the substance (150 nm for CB15, 800 nm for C15), but it is usually of the order of 10–20 wt.%. Compound mixing is performed at elevated temperatures near 70°C to promote dissolution of the chiral additive.

Table 21.I
Base nematics and chiral additives.

Nematics

$$X -\!\bigcirc\!- A - B -\!\bigcirc\!- Y$$

X, Y	A - B
Cyano-CN	Schiff-CH = N-
Alkyl-$CH_3(CH_2)_n$	Azoxy-N = N(O)-
Alkoxy-$CH_3(CH_2)_nO$	Ester-COO-

Merck: Licristal V, ZLI1646
BDH: E7, E8, ... E44
Roche: TN-403, TN701

LH Additives

COC
ZLI-811 } wax

C15
CN } powder

$$CH_3(CH_2)_7COOC_{27}H_{45}$$

RH Additives

CAA
S1082 } solid
CE1,2, . . . 7

CB15   fluid

$$CH_3CH_2\overset{\bullet}{C}HCH_2 -\!\bigcirc\!-\!\bigcirc\!- CN$$
$$\underset{CH_3}{|}$$

G1472

11

The recipe for circular polarizer fabrication is as follows:

(1) choose supporting substrate type (usually BK-7) and diameter (20–100 mm for present work);

(2) unidirectionally buff inner substrate surfaces with 1/10-μm diamond paste to create a preferred alignment direction and to provide wall anchoring for the liquid crystal molecules;

(3) heat substrates and tuned liquid crystal compound to ~70°C, apply 12-μm-thick Mylar spacer tabs, and form an air-gap sandwich;

(4) fill air-gap with heated fluid using capillary action;

(5) quench cell to room temperature and shear one substrate with respect to the other by 1/2 mm to orient the pitch structure along the beam propagation direction (see Fig. 21.9); and

(6) adjust cell for zero wedge in an interferometer and seal the fluid edge with epoxy.
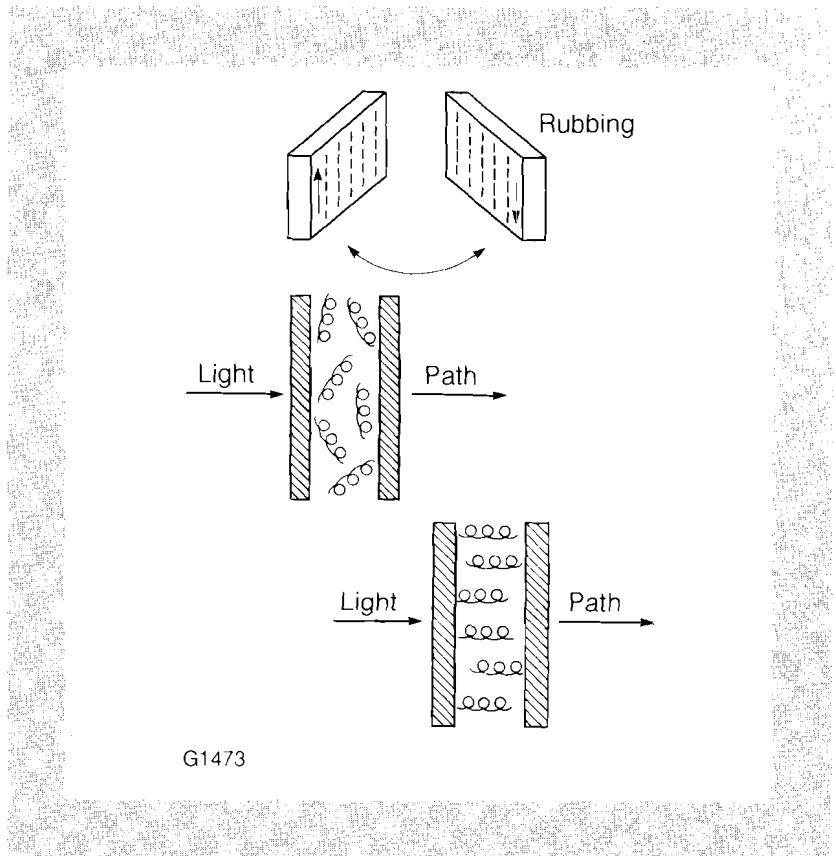
Fig. 21.9
Liquid crystal polarizer fabrication. Substrate inner surface rubbing helps to orient the rodlike liquid crystal molecules which contact the cell boundaries. A mechanical shear after the cell has been assembled tips molecular helices normal to the laser beam propagation direction, thereby minimizing scatter losses for the preserved polarization and maximizing extinction for the rejected polarization.

G1473

We have determined that fluid paths of 11–18 μm provide optimum polarization for the 1000-nm wavelength regime. The uniformity of fluid thickness across the polarizer clear aperture does not affect performance, as long as the layer exceeds a minimum of 10 pitch lengths. Transmission for the preserved polarization through a single element approaches 98%. Blocking extinction through crossed polarizers approaches 10^4.

The angular sensitivity of liquid crystal polarizers can be minimized by using base nematics whose birefringence Δn is large. Composition detuning to the long-wavelength side of the laser wavelength may also be employed to create polarizer elements whose angular performance resembles that shown in Fig. 21.10. Extinction from 0 to $\pm 20°$ off normal in excess of 10^3 has been demonstrated.
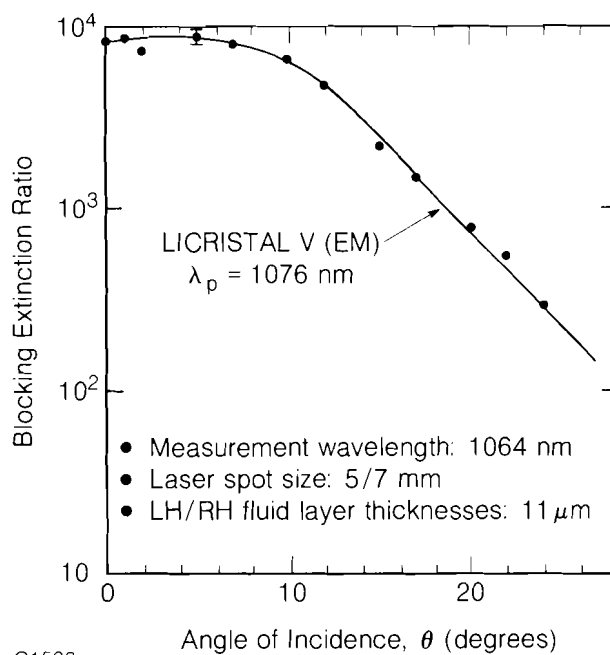
Fig. 21.10

Blocking extinction and angular sensitivity. Liquid fluid paths of between 11 and 18 μm are adequate to provide crossed polarizer blocking extinction levels of 10^4. The use of highly birefringent base nematics promotes selective reflection bandwidth in excess of 150 nm (FWHM). This in turn enables liquid crystal polarizers to be relatively insensitive to angle of incidence effects.

We have found that the temperature sensitivity of liquid crystal polarizers depends upon the type of base nematic and the type and quantity of chiral additive. Center-wavelength temperature shifts from 0.35 to 1.4 nm per °C have been measured. This level of sensitivity presents no problem to the use of these devices in our laboratory, where temperature is controlled to $\pm 3°C$.

A series of on-line laser damage tests was performed on 50- to 100-mm-diameter cells using the 1054-nm output of the GDL system. The RH combination of CB-15 in nematic E7 was found to be damage resistant to average fluences of 3 J/cm^2 (1 ns). LH polarizer cells failed at substantially lower fluences of less than 0.2 J/cm^2. Failure is determined by polariscopic observation of bubble growth in irradiated cells. We suspect that the primary reason for low damage thresholds in LH fluids is the lack of a room temperature, liquid chiral additive, or inadequate dissolution of the LH solid during fluid composition tuning. Our interim solution to this problem has been to employ RH element/half-wave-plate combinations to simulate the three LH elements indicated in Fig. 21.5.

A comparison of liquid crystal polarizers with other polarizer technologies is given in Table 21.II. Liquid crystals offer the advantages of high optical quality at large apertures, high contrast with angular insensitivity, high transmission for the preserved polarization, and environmental stability. They represent the only polarizer technology that, by itself, can provide back-reflection protection during standard use. Work is presently being conducted to understand and solve the LH-element, laser-damage problem.

Attribute	Crystal Prism	Brewster Thin Film	Dielectric Cube	Dyed Plastic	Liquid Crystal
• Optical quality at large apertures	no	yes	no	no	yes
• High contrast with angular insensitivity	no	no	no	yes	yes
• High transmission for passed polarization	yes	?	yes	no	yes
• Environmental stability	yes	no	yes	yes	yes
• Laser-damage resistance	some	yes	some	no	adequate
• Back-reflection protection	no	no	no	no	yes

G1479

Table 21.II
Comparison of polarizer technologies.

REFERENCES
1. S. D. Jacobs, K. A. Cerqua, T. J. Kessler, W. Seka, and R. Bahr, "Retrofit of a High-Power Nd:Glass Laser System with Liquid Crystal Polarizers," 16th Annual Symposium on Optical Materials for High-Power Lasers, Boulder, CO, 15–17 October 1984.

2. S. D. Jacobs, "Liquid Crystals for Laser Applications," in CRC Handbook Series of Laser Science and Technology, Vol. III, edited by M. J. Weber (in press).

3. S. D. Jacobs, SPIE Proceedings, Vol. 307: Polarizers and Applications, San Diego, CA, (1981), pp. 98–105.

4. S. D. Jacobs, J. A. Abate, K. A. Bauer, R. P. Bossert, and J. M. Rinefierd, Technical Digest – CLEOS/ICF'80, San Diego, CA (1980), pp. 128–129.

Section 2
PROGRESS IN LASER FUSION

2.A Simplified Theory of Electron Heat Transport

The kinetic theory of electron heat flow is an important topic in the study of laser-fusion plasmas.[1-13] As the laser drives a heat front into the plasma, temperature and density profiles become so steep that characteristic scale lengths become comparable to the collisional mean free paths of the electrons that dominate thermal conduction. Under these circumstances, the classical formulation of thermal conduction,[14] based on the random walk of electrons with mean free paths small compared to typical scale lengths, breaks down. The heat flow at any given radial position becomes dependent on the surrounding temperature and density profiles, and can be significantly inhibited or enhanced compared to its classical value. Such changes in the heat flow can significantly alter the hydrodynamic evolution of the plasma. These changes can also alter the smoothing of nonuniform laser energy deposition, which occurs as the nonuniformities are transported in from the critical to the ablation surface. Finally, the kinetic theory of nonclassical transport yields a non-Maxwellian electron distribution that can alter significantly the growth rates of magnetic instabilities,[15] which may, in turn, additionally affect thermal transport.

One approach to the transport problem has been to develop numerical codes that solve the full Fokker-Planck equation [1-4] (including such features as hydrodynamic motion, energy sources from inverse bremsstrahlung or resonant absorption, and energy losses from ablation). Because of restrictions on the time step in such codes, it has not been possible to use these codes to follow the hydrodynamics over realistic

time scales. Thus, other approaches, some predominantly analytic, make various simplifications in the Fokker-Planck equation;[5-13] with these models nonclassical heat fluxes are much more quickly obtained, and so may be more useful in a hydrodynamic code. One simplification, in particular, is to consider approximations appropriate to the behavior of "hot" electrons, which have velocities greater than about twice the average, or thermal, velocity.[6,7,10,12] [We define the thermal velocity as $(2T/m)^{1/2}$.] Such a model is motivated by the dominant role the hot electrons play in determining the heat transport. Here, we present some new studies and applications of such a model.

After describing our model, we consider, first of all, some of the questions of the self-consistency of our approximations. The model is then extended to three dimensions in order to study the smoothing of nonuniform energy deposition by electron transport. Finally, we develop our model heuristically to find an expression for the electron heat flux as a spatial convolution over nonlocal sources.[16]

Kinetic Model

The one-dimensional (1-D) Fokker-Planck equation for the electron distribution function $f(x, v, \mu, t)$,

$$\frac{\partial f}{\partial t} + \mu v \frac{\partial f}{\partial x} - \frac{eE}{m} \left[\mu \frac{\partial f}{\partial v} + \frac{1-\mu^2}{v} \frac{\partial f}{\partial \mu} \right] = \frac{\partial f}{\partial t}\bigg|_c , \quad (1)$$

is the basis for our work. Here x is the inhomogeneous dimension, $\mu \equiv \hat{\underline{v}} \cdot \hat{\underline{x}}$, and

$$\frac{\partial f}{\partial t}\bigg|_c$$

is the collision integral.[17] We analyze this equation as in the classical theory, expanding f in Legendre polynomials—here just the first two:

$$f(x, v, \mu, t) = f_0(x, v, t) + \mu f_1(x, v, t). \quad (2)$$

In this form f_0 represents the electron number and energy desnities, while f_1 represents the electron current and heat flux. Numerical work has shown[1,2] that this classical approach leads to accurate heat fluxes even for the steepest gradients encountered. We also take the steady-state limit, since the electron collision times are short compared to hydrodynamic time scales, and our source terms are independent of time. The electric field is determined by quasineutrality, which in 1-D steady state requires that the total current be zero, so that no charge accumulates at the boundaries of the plasma. Some further approximations are based on dividing the distribution into a small fraction of hot electrons and a bulk, or background, of cold electrons, which we take to obey the Spitzer-Härm solution. We then solve Eq. (1) for the nonclassical behavior of the hot electrons in the cold background. We also make the "high-Z" approximation, neglecting electron-electron collisions in comparison with electron-ion collisions, wherever possible, and further neglect electron-ion energy exchange.

With the preceding approximations, Eqs. (1) and (2) yield

$$-\frac{1}{v} \left(\frac{\partial}{\partial x} - \frac{eE}{mv} \frac{\partial}{\partial v} \right) (\lambda_0 v^6) \left(\frac{\partial}{\partial x} - \frac{eE}{mv} \frac{\partial}{\partial v} \right) f_0 = \frac{3}{2} \int_{-1}^{1} d\mu \frac{\partial f_0}{\partial t}\bigg|_c^{ee} \quad (3)$$

and

$$f_1 = -\lambda_o v^4 \left(\frac{\partial}{\partial x} - \frac{eE}{mv} \frac{\partial}{\partial v} \right) f_o. \qquad (4)$$

Here, $\lambda_o v^4$ is the mean free path for 90° scattering of an electron of velocity v by the combined angular scattering effects of ions and other electrons. The electron-electron collision term becomes

$$\left. \frac{\partial f_o}{\partial t} \right|_c^{ee} \approx \frac{1}{v^2} \frac{\partial}{\partial v} \left[f_o + \frac{T(x)}{mv} \frac{\partial f_o}{\partial v} \right], \qquad (5)$$

where $T(x)$ is the temperature of the bulk of the electrons. The first term in Eq. (5) is a drag operator, representing loss of energy from the hot electrons to the cold background; the second term diffuses the energy of the hot electrons in the relatively cold but finite background temperature. Equation (3) thus determines f_o through the balance of spatial diffusion and energy drag and diffusion from electron-electron collisions. Equation (4) describes the resultant flux, balancing the gradients of f_o with electron scattering off ions.

We further simplify our model by neglecting the electric field in Eq. (3), an assumption we verify á posteriori. The electric field is also neglected in Eq. (4) for the hot electrons but must be retained for the cold electrons.

Finally, we always make some approximation to the energy diffusion term in the electron-electron collision operator. This is a reasonable procedure when the tail of the distribution is "overfull," or overpopulated, regarding the Maxwellian distribution at the local temperature and density. The physical effect of the full electron-electron collision operator is then to drag the overpopulated tail down to the Maxwellian level, which is just what the drag operator alone tends to do. In fact, Fokker-Planck code results indicate that the electron distribution is overfull throughout most of the region where the heat flux is significant.

Self-Consistency of the Model

For simplicity, our first treatment of the energy diffusion term is to neglect it. We have then solved Eq. (3), neglecting the electric field, in the presence of a hot electron source, $\delta(x) \delta(v - v_h) (n_h / v_h)$, which corresponds to a source flux of electrons at $x = 0$, of energy $(mv_h^2/2)$, and whose strength is characterized by the density n_h. We refer to this as the monokinetic solution, which is clearly of general importance.

To check our neglect of electric field effects, we consider the ratio

$$R \equiv (eE/mv)(\partial f_o/\partial v)/(\partial f_o/\partial x),$$

of the term neglected to that retained in our calculation. The electric field is computed from Eq. (4) by setting the net current caused by the hot particles and Spitzer-Härm cold particles equal to zero. It is then found that R is insensitive to the exact value taken for v_o, the velocity dividing hot electrons from cold, provided $v_h^2 \gg v_T^2$ and $(v_h/v_o)^8 \gg 1$, where v_T is the thermal velocity. R is proportional to $(n_h v_h/n v_T)$, which represents the ratio of the normalizations of the hot-electron inward current to the cold-electron return current.

A typical plot of R is shown in Fig. 21.11 for $v_h = 3v_T$. The value given for $(n_h v_h / n v_T)$ is based on a numerical model of a penetrating heat front.[18] The electric field is typically found to be of negligible importance, compared with collisional effects, as in the figure. Only at much higher velocities do we find that R exceeds one. We do not, however, expect the transport to be sensitive to the behavior of the very small number of such particles [e.g., $(n_h/n) \sim 10^{-3}$ for $(v_h/v_T) \sim 7$].
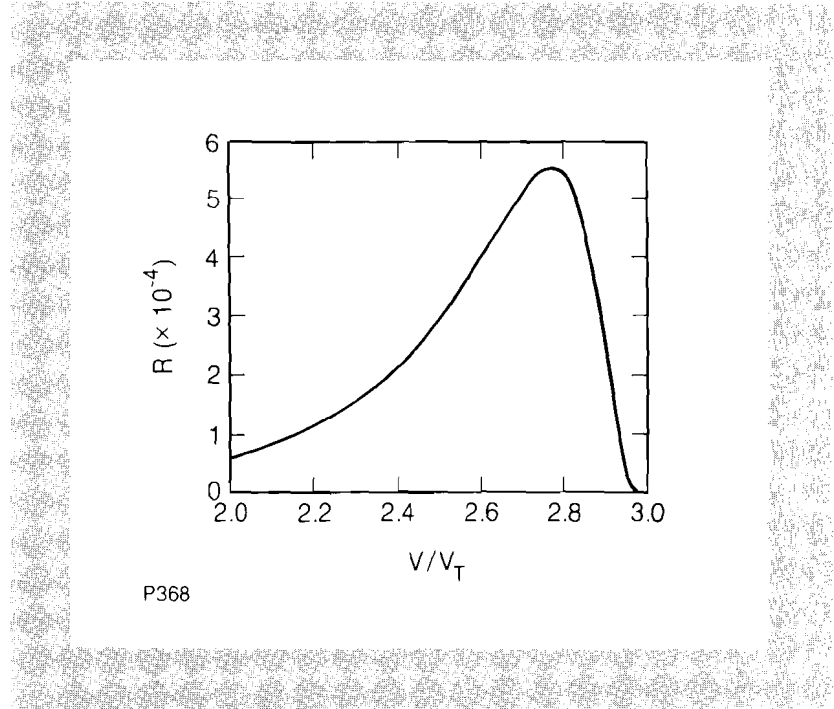
Fig. 21.11
Self-consistency of neglect of electric field in computation of hot-electron distribution. Ratio R of electric field term neglected to terms retained in Eqs. (3) and (4) is plotted. Case shown is for monokinetic solution with hot-electron source velocity $v_h = 3\,v_T$, $Z = 4$, and $(n_h v_h / n v_T) = 3.3 \times 10^{-3}$.

A second issue of self-consistency is the value of (f_1/f_0). If $(f_1/f_0) > 1$, f can become negative, while for $(f_1/f_0) > 3$, the distribution would imply that more than all of the particles are moving in one direction.[2,3] For the monokinetic solution, (f_1/f_0) is found to be proportional to $xv^4/(v_h^8 - v^8)$. Thus, (f_1/f_0) becomes large at large x and v, where there are the fewest particles, since particles are dragged to lower energies as x increases. [There are no particles at $v = v_h$, where (f_1/f_0) is singular.] Numerical computation confirms this behavior.

Smoothing from Electron Transport

To study smoothing, we generalize Eqs. (2)–(4) to three dimensions. Neglecting the electric fields, $(\partial^2/\partial x^2)$ is replaced by ∇^2 in Eq. (3), while $(\partial/\partial x)$ is replaced by $\hat{v} \cdot \nabla$ in Eq. (4), with μf_1 replaced by f_1 in Eq. (2). In the equation for f_0 we neglect magnetic fields, which can arise in three dimensions, as well as the electric field and the energy diffusion term. We also take the density to be constant, which is plausible for the foot, or preheat, region of a heat front. As a model for nonuniform energy deposition, we consider a source $S^{(1)}$ localized at $x = 0$, with plane wave behavior in the transverse directions, and a Maxwellian distribution in $v, S^{(1)} = A\delta(x)\, e^{ik_y y}e^{ik_z z}\exp(-v^2/v_h^2)$ with

$$A = n^{(1)}(\pi^{1/2}v_h)^{-3}.$$

In practice, $S^{(1)}$ is a small perturbation on the zero order source and yields a corresponding perturbation in f_0, $f_0^{(1)}$. Both f_0 and $f_0^{(1)}$ are easily reduced to quadrature.

With $f_0^{(1)}$ we study the radial smoothing of the energy density,

$$\epsilon^{(1)} = n^{(1)}T^{(1)} = \int d^3v \, \frac{mv^2}{2} \, f_0^{(1)} \,, \tag{6}$$

and of the energy deposition rate $\dot{Q}^{(1)}$ which is determined by the drag operator in the equation for f_0,

$$\dot{Q}^{(1)} = \frac{2\pi m}{\lambda_0 \, (z+1)} \int_0^\infty dv \, v^2 \frac{\partial}{\partial v} \, f_0^{(1)} \,, \tag{7}$$

where z is the ion charge. (We have extended the integrals to $v = 0$, since their behavior is dominated by the high-energy contributions.) An analytic estimate[10] of $\epsilon^{(1)}$ indicates that $\epsilon^{(1)} \propto H(\lambda(x) - x)\exp(-k_\perp x)$, where $\lambda(x)$ is the velocity-averaged, energy-loss mean free path and H is the Heaviside step function. These two factors represent the intrinsic smoothing of the transverse variation and the loss of energy to the cold background. When $k_\perp \lambda$ is less than one, the smoothing factor $e^{-k_\perp x}$ has little effect, while for $k_\perp \lambda$ greater than one it is dominant. This behavior is approximately verified by the numerical evaluations of $\epsilon^{(1)}$ and $|\dot{Q}^{(1)}|$ shown in Fig. 21.12. The specific case considered is the same as the one in Ref. 7, i.e., the material is gold and the hot-electron temperature is 10 keV. The dimensionless unit of length in Fig. 21.12 corresponds to 0.041 μm at solid density (19.5 g/cm^3). From the figures we see the $e^{-k_\perp x}$ behavior of $\epsilon^{(1)}$ emerge as $k_\perp$ increases. The ratio of slopes for the straight line figures approximately corresponds to $e^{-k_\perp x}$ behavior. Furthermore, as x increases the curves asymptotically approach this behavior, since $\lambda(x)$ increases with x as the distribution $f_0^{(1)}$ becomes weighted toward higher energies. The figures of $|\dot{Q}^{(1)}|$ display the same qualitative behavior as the $\epsilon^{(1)}$ figures, amplified by the fact that they result from higher velocity moments of the distribution.

Formulation of Delocalized Heat Flow

Returning to Eq. (3), we develop a heuristic model for nonlocal thermal conduction in steep temperature gradients. For this purpose the energy diffusion term must be retained in some form to account for the effect of a given temperature profile T(x). We include it by taking

$$f_0 = f_M = [n(\ell)/\pi^{3/2}v_T^3(\ell)]\exp[-v^2/v_T^2(\ell)]$$

in the diffusion term. This formulation guarantees that in the limit of high collisionality the Spitzer-Härm limit, $f_0 = f_M$, is recovered. We also neglect all explicit electron energy sources and sinks. We neglect the electric field in Eq. (3), but retain it in Eq. (4), so that we can extend the resulting distribution to all velocities. The resulting expression for the heat flux q is easily obtained from Eqs. (3)–(5). This heat flux is in the simple form of a convolution of sources propagated from all points along the heat front.

The appropriate physical properties of the nonlocal heat-flux formula are easily verified. In the limit of high collisionality (or, equivalently, weak

P369
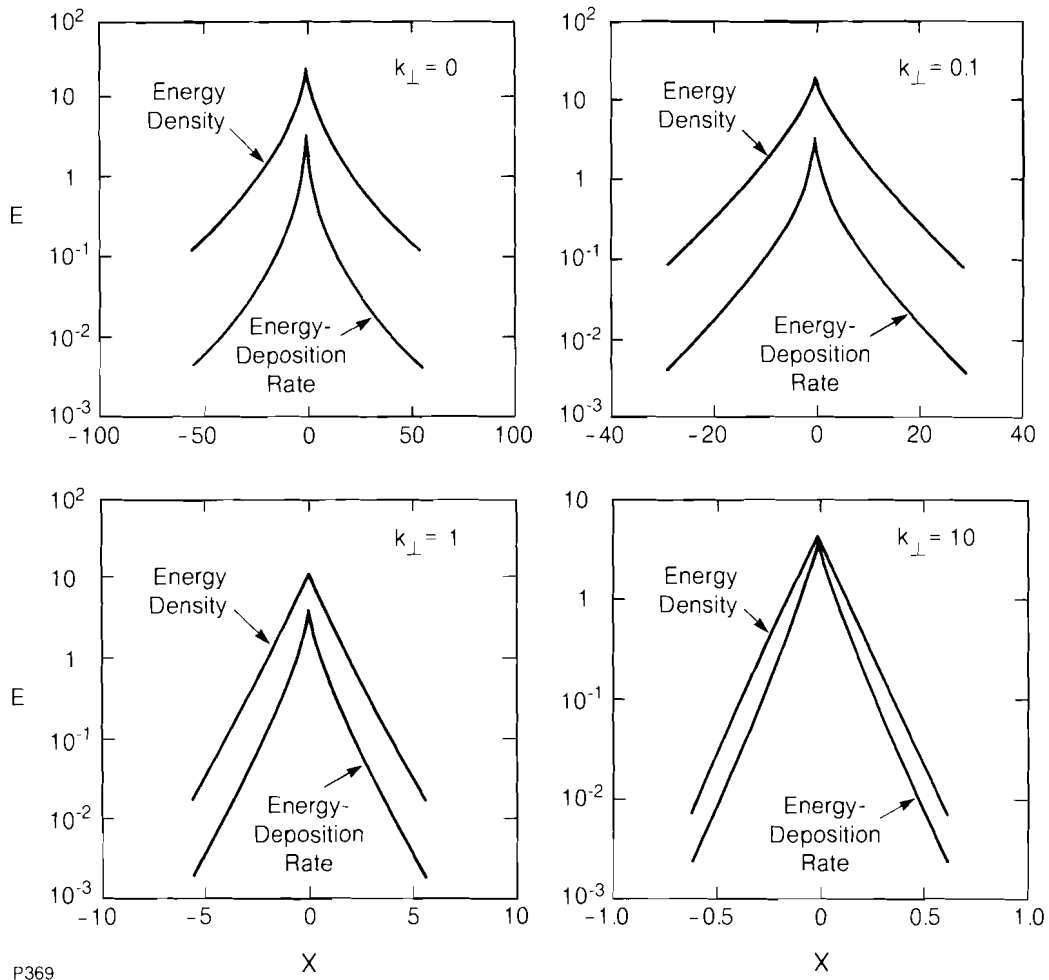
Fig. 21.12
*Radial smoothing of nonuniform energy
deposition. The perturbed hot-electron
energy density $E^{(1)}$ and the perturbed hot-
electron energy deposition rate $\dot{Q}^{(1)}$ are
plotted for a δ-function source at x = 0. The
unit of length is the geometric mean of the
mean free paths and $k_\perp$ is the magnitude
of the transverse k-vector of the perturba-
tion. The $k_\perp = 0$ case is identical to the
zero-order heat transport case. At $k_\perp = 10$,
the wavelength of the perturbation com-
pletely controls the heat penetration.*

gradients in n and T), the classical result is recovered. In the limit of an
infinitely steep temperature gradient, a "flux-limited" heat flux is
computed,

$$q \rightarrow \frac{1.4}{(Z+1)^{1/2}} q_{FS} \text{ ,}$$

where $q_{FS} \equiv nT(T/m)^{1/2}$ is the free-streaming heat flux. This result is
always less than q_{FS} and can be reduced further by including the effect
of electron-electron collisions in Eq. (4), which leads to an additional
factor of $(Z+0.24)(Z+4.2)^{-1}$; for example, $q \rightarrow (0.3)q_{FS}$ for z = 5.

Summary

We have developed a simplified electron thermal transport theory and
have found this model to be self-consistent in some important respects.
A simple generalization of the model to study smoothing indicates that
transverse nonuniformities in energy density and heat flux decay as
$\exp(-k_\perp x)H(\lambda(x) - x)$. Different smoothing behavior may depend on the
inclusion of magnetic field effects on the hot particles,[19] or effects of the

electric field on the intermediate velocity particles, which have not been included here.

A heuristic generalization of our model gives the heat flux as a nonlocal convolution of given density and temperature profiles. Unlike a similar published result,[11] our formula is independent of any arbitrary or phenomenological parameters.

Continuing work on our model[20] includes comparison of our heat flux results to those of a full Fokker-Planck code. We are also increasing the efficiency of numerical evaluation of our formula for the heat flux; this will allow computation of temperature and density profiles from the time-dependent hydrodynamic equations.

ACKNOWLEDGMENT

REFERENCES

1. A. R. Bell, R. G. Evans, and D. J. Nicholas, *Phys. Rev. Lett.* **46**, 243 (1981).

2. J. P. Matte and J. Virmont, *Phys. Rev. Lett.* **49**, 1936 (1982).

3. J. R. Albritton, *Phys. Rev. Lett.* **50**, 2078 (1983).

4. J. P. Matte, T. W. Johnston, J. Delettrez, and R. L. McCrory, *Phys. Rev. Lett.* **53**, 1461 (1984).

5. D. Shvarts, J. Delettrez, R. L. McCrory, and C. P. Verdon, *Phys. Rev. Lett.* **47**, 247 (1981).

6. J. R. Albritton, C. J. Randall, and A. B. Langdon, Laser Program Annual Report – 1981, LLNL Report UCRL-50021-81, p. 3–44.

7. E. L. Lindman, 1981 CECAM Report, p. 113.

8. D. Shvarts, J. A. Delettrez, and R. L. McCrory, 1981 CECAM Report, p. 47.

9. Y. Kishimoto and K. Mima, *J. Phys. Soc. Jpn.* **52**, 3389 (1983).

10. K. Swartz and E. A. Williams, *Bull. Am. Phys. Soc.* **28**, 1246 (1983).

11. J. F. Luciani, P. Mora, and J. Virmont, *Phys. Rev. Lett.* **51**, 1664 (1983).

12. J. F. Luciani, P. Mora, and R. Pellat, Centre de Physique Theorique, Ecole Polytechnique, preprint A570.0983 (1983).

13. P. M. Campbell, *Phys. Rev. A* **30**, 365 (1984).

14. L. Spitzer and R. Härm, *Phys. Rev.* **89**, 977 (1953).

15. E. M. Epperlein and M. G. Haines, 1982 CECAM Report, p. 211.

16. A. R. Bell, *Phys. Fluids* **26**, 279 (1983).

17. I. P. Shkarofsky, T. W. Johnston, and M. P. Backynski, *The Particle Kinetics of Plasmas* (Addison-Wesley, Reading, Massachusetts, 1966).

18. J. Delettrez (private communication).

19. M. Strauss, G. Hazak, D. Shvarts, and R. S. Craxton, 1982 CECAM Report, p. 174; LLE Review **16**, 17 (1983).

20. K. Swartz, R. W. Short, and J. R. Albritton, *Bull. Am. Phys. Soc.* **29**, 1326 (1984).

2.B Aluminum/Aluminum-Nitride Sputter Deposition on the Inertial Fusion Target Using the Pulsed-Gas Process

Typical inertial confinement fusion targets consist of hollow glass microballoons (GMB's) of submillimeter diameter filled with pressurized DT gas. They are often coated with organic, and/or metal layers, and for successful implosion of these targets, high spherical symmetry and uniformity of the coating are essential. Variation in thickness and density of the coated layer should be less than a few percent and the rms surface finish less than 500 Å. Conventional techniques for metal coating using sputtering or evaporation do not provide these criteria due to the inherent, oblique incidence of the coating flux and poor control of substrate temperature in these processes. Depositions of aluminum have particularly poor surface morphology and low bulk density due to the columnar crystal growth[1] of an aluminum film.

A number of techniques have been extensively investigated as methods of obtaining smooth surface finishes and sufficient density uniformity of metal films. These include biased magnetron sputtering,[2] ion cluster beam coating,[3] and pulsed-gas sputtering processes.[4] Biased sputter coating has been employed in the coating of metal pusher layers onto inertial fusion targets to improve surface morphology. Ion cluster beam deposition also produces smooth, dense coating layers by accelerating an ionized cluster of loosely bound atoms into a substrate. This process has yet to be adopted for coating GMB's. Periodic pulsing of N_2 or O_2 during the sputtering process has been shown to form alternating layers of metal and metal nitride or metal oxide.[4] This technique suppresses columnar growth, produces high-yield-strength materials, and provides smooth surface finishes. To date this method has been applied to flat and cylindrical substrates, but we are unaware of any previous application of this technology to metal layer coatings on GMB's.

The present manuscript describes the application of the pulsed-gas process to coat pusher layers into glass microballoons to be used as fuel containers in inertial fusion experiments at LLE. In our experiment, aluminum was chosen as the coating material in the magnetron sput-

tering. An aluminum coating generally lacks high bulk density and displays rough surfaces, with frequent voids in the film. The effect of pulsed-gas processes in aluminum coatings is very pronounced.

Deposition of aluminum coatings was performed in a vacuum system consisting of a stainless steel chamber pumped by an Edwards cryo-baffled 15-cm diffusion pump. The sputtering source was a Sloan S-310 magnetron sputter head. Argon sputter gas was purified in an R. D. Mathis gas purifier, and dry nitrogen was supplied from a liquid nitrogen gas phase line. An MKS-260 pressure controller was used with MKS-260 valves, an MKS-260 flow transducer, and an MKS-227 Baratron pressure gauge. Base pressure prior to coating was in the range of 10^{-4} Pa. The argon and nitrogen flows were set at 3.0 sccm, and the magnetron sputter head was operated at a dc current of 1.0 A. The nitrogen pulsing period was varied depending on the thickness to be coated. For coatings less than 2-μm thick, pulsing for 25 s every 3 min was satisfactory, that is, the density of the film and the surface finish were much improved compared with the aluminum coating without pulsing. During the nitrogen pulsing period, the flow rate of N_2 was kept as 3.0 sccm. For coatings up to 5 μm in thickness, pulsing for 2 s every 15 s was sufficient. At lower pulsing rates, the film tended to peel from the substrate.

Pulsed-gas processes have successfully been applied to produce high-yield-strength materials by forming alternating thin layers of high- and low-shear modulus materials. The effect of thin alternating layers is to inhibit the dislocation formation and the mobility of the dislocations, thus providing for improved mechanical properties. In addition, effective periodic inclusion of impurities as a result of this process improves specularity of the film surface substantially; it is this property that is of the utmost importance to us.

The effect of nitrogen pulsing on aluminum sputter coatings is shown in Figs. 21.13(a) and 21.13(b). Figure 21.13(b) is a scanning electron

Fig. 21.13
Scanning electron micrographs of sputter-deposited aluminum film (a) and aluminum deposit using a pulsed-nitrogen process (b). Frequency of pulsing was 25-s injections at 3-min intervals. Film density and surface finish are shown to be much improved by the pulsing.
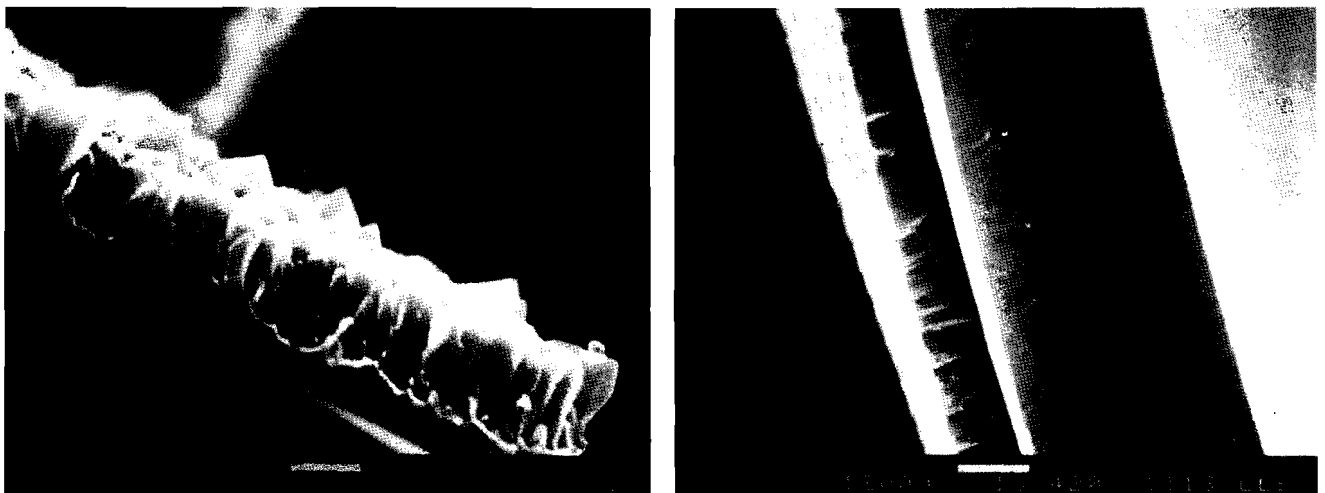
T667 (a)   (b)

micrograph of a 1-μm-thick Al coating that was obtained with N_2 pulses of 25 s injected at 3-min intervals. Compared with Fig. 21.13(a), which shows the structure of pure aluminum deposit, the effect on surface finish and on the removal of voids is dramatic. A careful examination of these photos reveals that the structure obtained with the N_2 pulsing process is not columnar, in contrast to pure deposit, nor lamellar. This observation is at variance with the published reports that describe a formation of alternating layers of pure deposit and aluminum nitride. Under conditions in the present experiment, the coating rate is 140 Å/min. A 25-s N_2 pulse duration at 3-min intervals implies deposition of alternating layers of 58-Å-thick aluminum nitride and 360-Å-thick aluminum. These dimensions are too small to be measured by a scanning electron microscope. Moreover, the profile of nitrogen injection is not a step function but one resembling a sinusoidal shape. The net result is to make deposition of nitrogen atoms more or less uniform into the aluminum matrix.

The surface finish does not appear to depend on the N_2 pulsing period. Figure 21.14(a) is surface morphology when N_2 gas was pulsed for 2 s in 12-s intervals. The surface finish of Fig. 21.14(a) is qualitatively the same as that of Fig. 21.13(b), which was obtained at a pulsing rate of 25 s in 3-min intervals. The amount of nitrogen gas injection is the same in both cases but the injection rate was different. A grain in Fig. 21.14(a) is magnified in Fig. 21.14(b), where its fractured cross section is magnified to show that the height of the grain is less than 0.1 μm.

Fig. 21.14
Aluminum film at nitrogen pulsing of 2 s in 12-sec intervals. Left photograph (a) shows an edge view of the film, while the right photograph (b) shows peak-to-valley dimensions of a major defect to be ≈50 nm.

(a)

T740

(b)
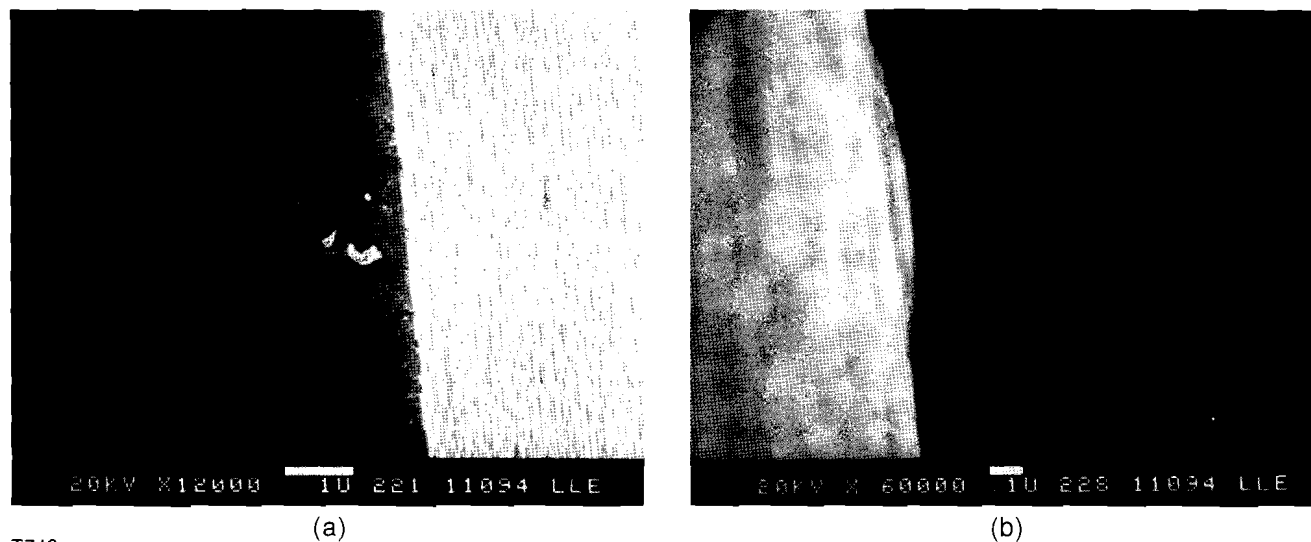
The structure and composition of the N_2-pulsed aluminum coatings were studied by x-ray diffraction and an energy-dispersive x-ray analysis technique. The x-ray diffraction scan was obtained by a Riguku diffractiometer; the results are shown in Fig. 21.15. Also depicted in Fig. 21.15 is the stick diagram of aluminum nitride, AℓN. The diffraction peaks are very shallow except for the one that appears at $2\theta = 36.7°$. Furthermore, comparison with the stick diagram of AℓN shows that the broad peaks of the diffraction pattern coincide with the combination of the peaks in the diagram. This implies that the main component of the
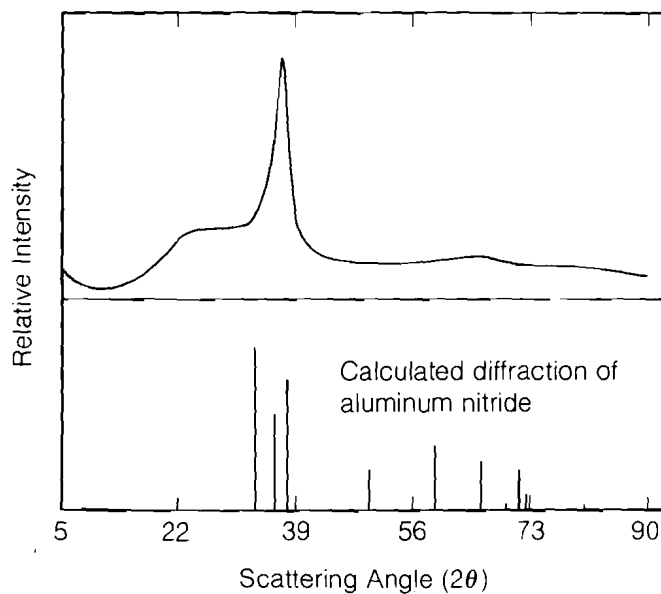
Fig. 21.15
X-ray diffraction pattern of a pulsed Al
coating. The lower figure shows a stick
diagram of aluminum nitride standard.

N_2-pulsed aluminum coating consists of very small crystallites of aluminum nitride. The broad peak near $2\theta = 22°$ may be that associated with the amorphous phase.

The chemical composition of the film was studied by an energy-dispersive x-ray analysis method using an EDAX unit. Figure 21.16 shows the energy-dispersive analyses of aluminum coatings with and without nitrogen pulsing. These two peaks are normalized to Al peaks. As expected, the presence of N_2 was detected from the scan of the nitrogen-pulsed peak. The content of nitrogen incorporation is believed to be less than 5 atomic %. The small oxygen peak appearing in both scans is due to the oxidation of the film when exposed to air.

In the pure Al deposit without N_2 pulsing, the oblique incidence of the flux of sputtered aluminum atoms causes self-shadowing, surface roughness, and voids, thus forming brittle coatings. Further, columnar growth, a characteristic crystal growth habit of thin-film deposition, also contributes substantially to the poor surface finish and inferior mechanical properties. When nitrogen ions, which can be considered defect-forming impurities, are periodically injected onto growing crystallographic planes, they poison the growth; therefore, ordinary dendritic crystallization cannot proceed. Deposit of nitrogen ions may become new heterogeneous nucleation sites. Under such conditions, either grain refinement occurs or an amorphous structure forms.

Although the injection of nitrogen gas is by perodic pulsing, it is not an abrupt on-and-off switching but resembles a sinusoidal shape. The net result is that nitrogen incorporation is more or less continuous. This precludes the possibility of forming alternating layers of aluminum and

25
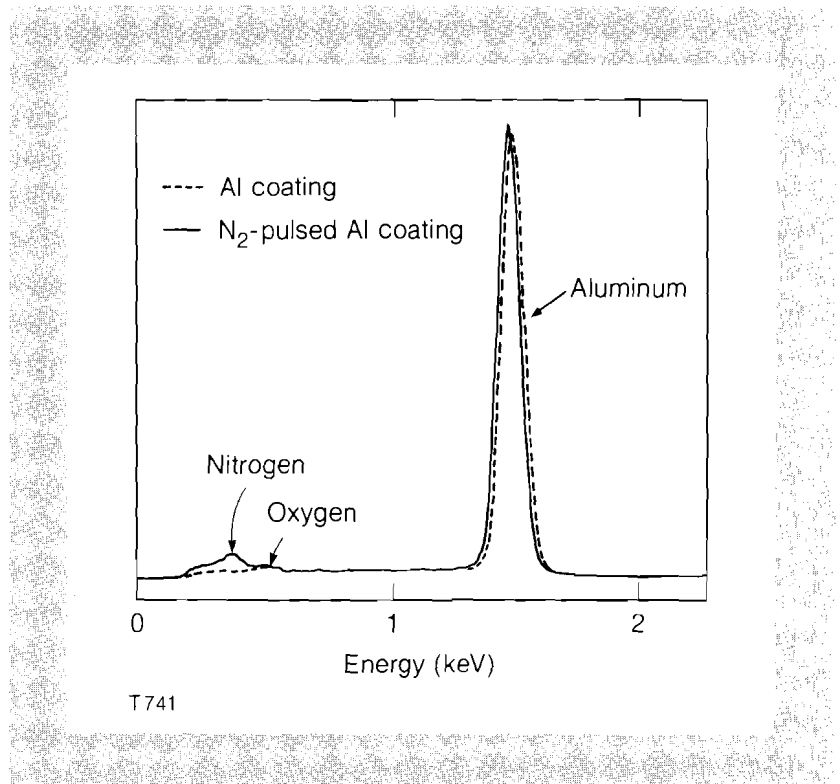
Fig. 21.16
An energy dispersive spectroscopy analysis of both pulsed aluminum and unpulsed pure aluminum. The pulsed sample is shown as a solid line; the unpulsed, a dotted line. The pulsed sample was normalized to pure aluminum peak.

aluminum nitride. It has been reported that epitaxial single-crystal growth of aluminum and aluminum nitride layers is a structure obtained by aluminum pulsing process and that this structure is responsible for high-yield strength. However, Fig. 21.16 indicates that the amount of nitrogen ions incorporated into the film is small, and our x-ray studies show that the structure is essentially amorphous. It is therefore concluded that the improved surface finish we obtained is due to the amorphous structure of the film.

ACKNOWLEDGMENT

REFERENCES

1. S. F. Meyer, *J. Vac. Sci. Technol.* **18**, 1198 (1981).

2. D. Glocker, *J. Vac. Sci. Technol.* **A-1**, 880 (1983).

3. T. Takagi, K. Matsubara, and H. Takaoka, *J. Appl. Phys.* **51**, 5419 (1980).

4. R. W. Springer and C. D. Hosford, *J. Vac. Sci. Technol.* **20**, 462 (1982).

5. R. W. Springer and D. S. Catlett, *Thin Solid Films* **54**, 197 (1978).

6. R. W. Springer, B. L. Barthell, and D. Rohr, *J. Vac. Sci. Technol.* **17**, 437 (1980).

Section 3
ADVANCED TECHNOLOGY DEVELOPMENTS

3.A   Multibeam, Laser-Imploded Cylindrical Plasmas

Many proposed x-ray laser schemes incorporate a linear, high-density, high-temperature plasma generated by a cylindrically focused beam, or by multiple spherically focused beams from a high-intensity laser.[1] For the plasma to be optimum as an x-ray laser medium, it should not only have density and temperature conditions appropriate for maximum population of the x-ray laser ion states, but also a geometric shape and uniformity of plasma conditions conducive to providing high x-ray gain along the axis of the plasma. Most experimental studies of collisionally excited or recombination x-ray laser schemes have so far used expanding plasmas created by focusing a laser on a solid target. The characteristics of such plasmas produced by spherically focused laser beams have been investigated in great detail because of their application to laser-fusion studies; plasmas created by cylindrically focused laser beams have not been examined so thoroughly.[2] In many respects, plasmas produced by short, intense laser pulses focused on solid massive targets are not ideal for x-ray laser schemes. These plasmas have steep density and temperature gradients across which ion state populations are rapidly varying, making the conditions for x-ray gain highly transient. Moreover, refraction of x rays on the plasma density profile can contribute to a reduction in gain. These detrimental factors are compounded by the microscopic variations produced in the plasma profile by the small-scale variations in the intensity profile of most focused laser beams. These limitations can be alleviated with simple changes to the target design.

One approach to producing a more uniform plasma in which the effects of nonuniformities in the irradiating beam are smoothed out is to form the plasma from an exploding thin foil. This may be achieved effectively by suprathermal electrons generated by resonance-absorption in interaction with a short-pulse (≤ 100 μm), intense ($> 10^{14}$ W/cm^2), long-wavelength (> 1-μm) laser. Similar conditions may be achieved with intense, short-wavelength radiation where rapid decompression of the foil results from shock and radiational heating. Alternatively, targets consisting of low-density material ($n < n_{solid}$) may also be good candidates for x-ray laser media, although the effects of self-induced, whole-beam self-focusing may have to be taken into account.

We describe here two novel approaches to the development of a linear uniform medium suitable for x-ray gain conditions. Both these approaches depend upon the ability to uniformly compress cylindrical targets with multiple, line-focused laser beams. Here, we present some initial investigations of these approaches performed with four line-focused beams of the upconverted 351-nm OMEGA facility.[3] The four beams, each producing ~50 J in ~600 ps, were focused orthogonally onto the cylindrical target (Fig. 21.17) by an f/3.7 fused silica lens combination comprising a high-power aspheric singlet lens and a close-coupled spherical cylindrical corrector plate. The focused beams produced a line focus of length 1700 μm and width ≥ 50 μm. Average irradiation intensities of ~10^{14} W/cm^2 were produced when the beams were focused onto 100-μm-diameter targets with the four orthogonal beams tangentially overlapping the target. The four beams were co-aligned with aid of a reflective solid cylindrical surrogate target, from

Fig. 21.17
Four-beam compression of cylindrical targets with 351-nm, four orthogonal line-focused beams of OMEGA.

Two-element fused-silica focusing system
f/3 aspheric focusing element
f/40 cylindrical correctors

351-nm input
Energy ~ 50 J
600 ps

Cylindrical shell target
2-mm long
100-μm diameter

E3132
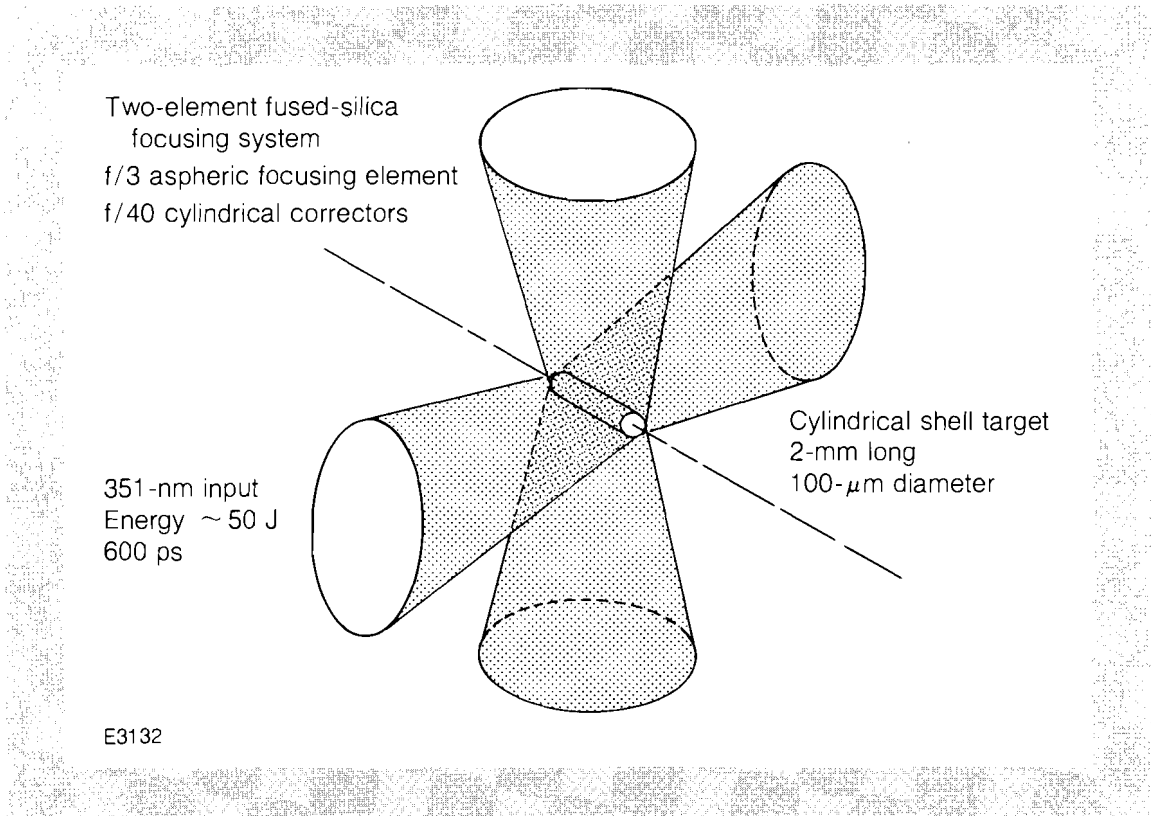
which fiducials were transposed to fixed high-resolution viewing systems for positioning the irradiated targets. Individual beams were aligned in position to an accuracy of ~20 μm and were oriented parallel to one another within ~10^{-2} radians. The axis of the cylindrical target could be set to an axis fixed to the enclosing vacuum chamber to an accuracy of 3×10^{-3} rad.

Two types of imploding targets were investigated, and they were compared to a solid Al cylinder target (see Fig. 21.18). The first, shown in Fig. 21.18(a), comprised a 100-μm-diameter CH cylindrical shell, 3- to 5-μm thick, and the inside of the shell was coated with a 0.3-μm-thick layer of Al. The CH in this target serves as an ablator, and its thickness was chosen to equal the ablation depth for an intensity of ~10^{14} W/cm^2. Thus, the Al layer is subjected to minimal heating until it stagnates at the center of the target. Cylindrical, 1-D (*LILAC*) Lagrangian hydrodynamic code calculations indicate the Al reaches final density and temperature of 10^{22} cm^{-3} and ~500 eV, respectively, over an extent of ~40 μm. Being ablatively driven by short-wavelength radiation, this target is sensitive to irradiation nonuniformities resulting from the use of only four beams. The final core density is higher than optimum for most soft x-ray laser schemes. This can be reduced by coating a thin (~0.015-μm), high-Z (Au) material on the outside of the CH shell. The initial burst of x-ray emission from the Au shell penetrates the CH and preheats the Al before it is compressed. The resulting in-flight decompression of the Al should reduce the final core density without leading to a reduced core temperature.

(a)
Ablatively Driven Shell

(b)
Compressed Exploded Shell

Void (100 μm)
Al (0.3 μm)
CH (3-5 μm)
Au (0.015 μm)

Void (100 μm)
Al (0.3 μm)

E3133
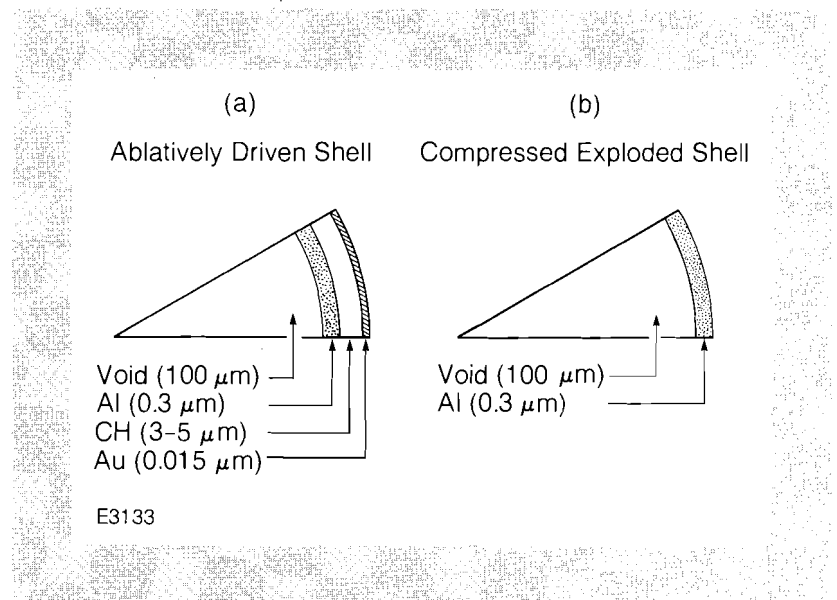
Fig. 21.18
Cylindrical shell targets investigated for the production of linear high-density, high-temperature plasma conditions.

The second type of cylindrical target is shown in Fig.21.18(b). This consists of an ultrathin (0.3-μm) Al cylinder of 100-μm diameter.[4] Upon irradiation, this shell quickly explodes and, according to *LILAC* calculations, the decompressed shell is rapidly imploded. Following stagnation of the implosion, the high-temperature core unloads radially, producing a cylindrical, high-temperature plasma (Fig. 21.19). From Fig. 21.19, it can be seen that two regions of the plasma possess parameters suitable as an x-ray laser medium. The narrow central region reaches densities
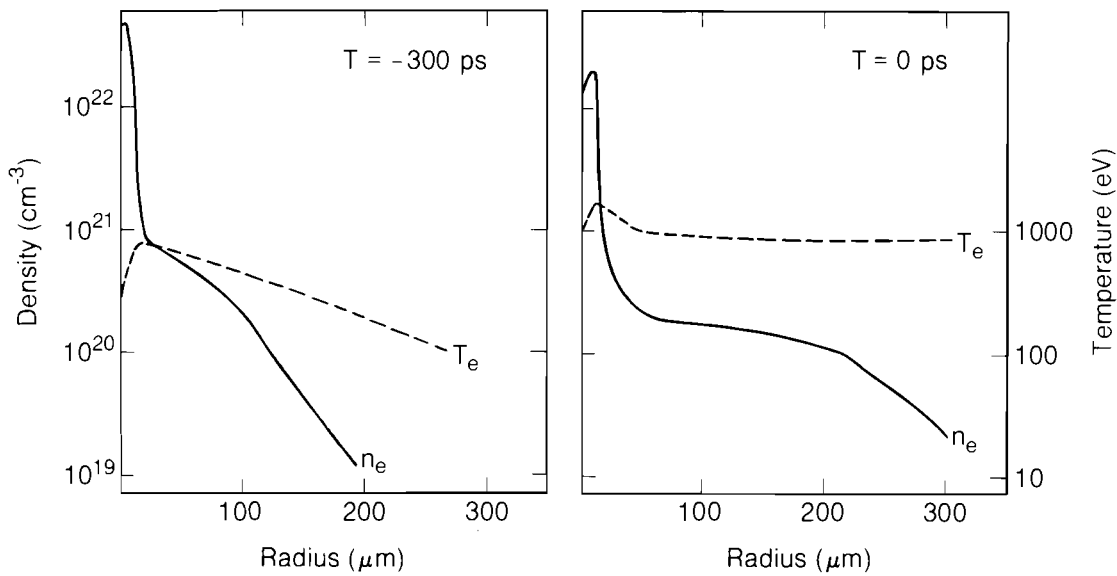
Fig. 21.19
Density and temperature profiles predicted by the 1-D code LILAC for the thin Al cylindrical target shown in Fig. 21.18(b).

higher than 10^{22} cm^{-3} over a radial extent of 10–20 μm with a temperature of several hundred electron volts. Although the code predicts a minimum in the electron temperature on axis, it is likely that the temperature in this region would be smoothed by small-scale inhomogeneities. This high-density, high-temperature region persists for some time ($\sim$ 100 ps) following the implosion, and, therefore, offers a potentially optimum medium for x-ray amplification. The underdense region of the plasma is maintained by flow of plasma from the dense core. Under the influence of continuing absorption during the remainder of the laser pulse, a long, radially expanding plateau of plasma having an electron density larger than 10^{20} cm^{-3} is produced. Almost stationary in profile, and with an electron temperature approaching 1 keV, this plasma provides conditions generally considered optimum for collisional excitation or recombination-pumped laser schemes.

Several experiments were performed with the four orthogonally oriented, line-focused, 351-nm beams of the OMEGA system using the targets depicted in Fig. 21.18, and the results were compared with those of the experiments using uniformly irradiated, solid Al cylindrical targets of the same diameter. Diagnostics included plasma calorimetry, x-ray photography, time-integrated x-ray spectroscopy, and time-resolved x-ray spectroscopy.

Absorption was measured with an approximately isotropic array of 20 plasma-calorimeters. These registered a uniform plasma blow-off distribution, with overall absorption of $\sim$ 50% for the solid and ablatively driven cylinders, and typically $\sim$ 44% for the thin Al cylinders. This is about a factor of 2 less than that measured for spherical targets at this intensity. Excluding the possibility that there is a higher plasma blow-off

along the axis, which was not measured, this implies that a considerable fraction of the beam energy was missing the target. Apart from x-ray photography studies of the extent of the line focus, no optical measurements of the focal distribution have been made. From previous studies of line focus distributions,[2] an intensity distribution in which about half of the energy is in a broad, low-intensity component is not unexpected.

X-ray image data of these types of targets irradiated are shown in Fig. 21.20. The x-ray image of the solid Al target [Fig. 21.20(a)] qualitatively indicates the apparent uniform illumination of the target in cylindrical geometry. Figure 21.20(b) shows the x-ray image of an ablatively driven Al shell. Weak x-ray emission from the core of the imploded shell can be observed. However, its uniformity along the 2-mm length of the target is poor, as is the linearity of the compressed core. Figure 21.20(c) shows the x-ray image of a compressed, thin (0.3-μm) Al shell. The resulting x-ray emission (0.8–1.2 keV) is uniform and collinear with the original cylinder axis, and its radial extent ($\sim$ 25-μm diameter) is in good agreement with the *LILAC* predictions.

(a)

(b)

(c)

| 1 mm |
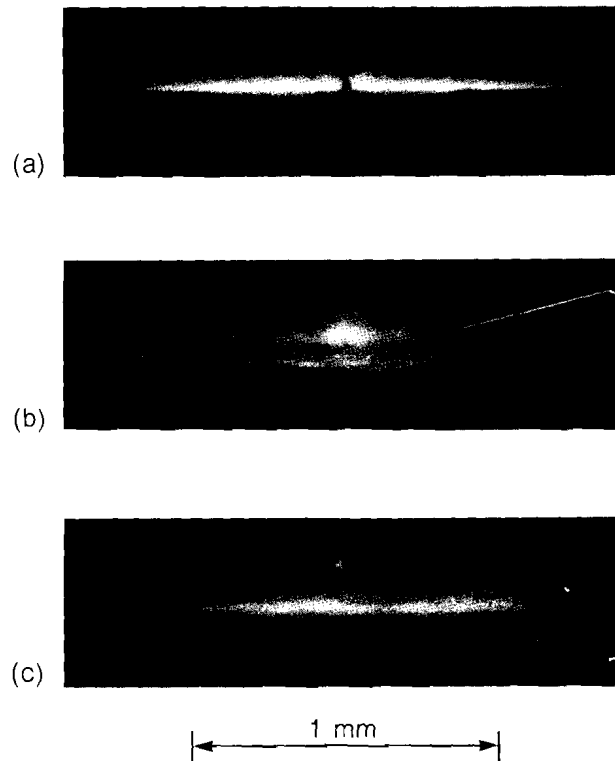
Fig. 21.20
X-ray photographs of three types of cylindrical targets irradiated by four orthogonal beams of OMEGA.
(a) a solid Al cylinder of 100-μm diameter,
(b) an ablatively driven plastic shell having a thin, linear Al shell, and
(c) a 3000-Å, thin Al shell of 70-μm diameter.

E3134

The overall relative x-ray conversion was measured with the low-energy channels (E < 3 keV) of a 15-channel, K-edge-filter pin diode/photomultiplier-scintillator x-ray continuum spectrometer. Assuming isotropy of x-ray emission, the x rays from the CH ablative target, the Al-coated ablative target, the thin Al target, and the solid Al target were in the ratio 0.02:0.1:1.3:1.0. Time-resolved x-ray spectroscopic studies of the x ray emitted from the line plasma were made with two streak spectrographs.

A streak transmission-grating spectrograph[5] comprising a freestanding Au bar grating (period 3000 Å, and thickness ~1 μm) displayed first-order spectral emission in the range 1–30 Å across the Au on CH soft x-ray photocathode of a streak camera. The second time-resolved spectrograph is sensitive in the 5- to 7-Å region and consists of an elliptical crystal dispersive element in conjunction with a CsI-on-Be photocathode-streak camera. The time resolution of both units is <20 ps.[6] Figure 21.21 shows typical spectra from the latter instrument for two types of cylindrical targets: a solid Al cylinder target and a thin Al shell cylinder. The He-like and H-like resonance line emission is evident in both spectra. The emission from the solid cylinder results from coronal plasma ablating from the target, and its duration is consequently of the same order as the laser pulse duration. The duration of the x-ray line emission from the imploding Al cylindrical target is significantly shorter (~150 ps). The major part of the x-ray emission occurs before the peak of the laser pulse, the implosion of the shell occurring on the rising edge of the pulse. Detailed analysis of these spectra is planned to obtain greater characterization of the plasma conditions.

E3131
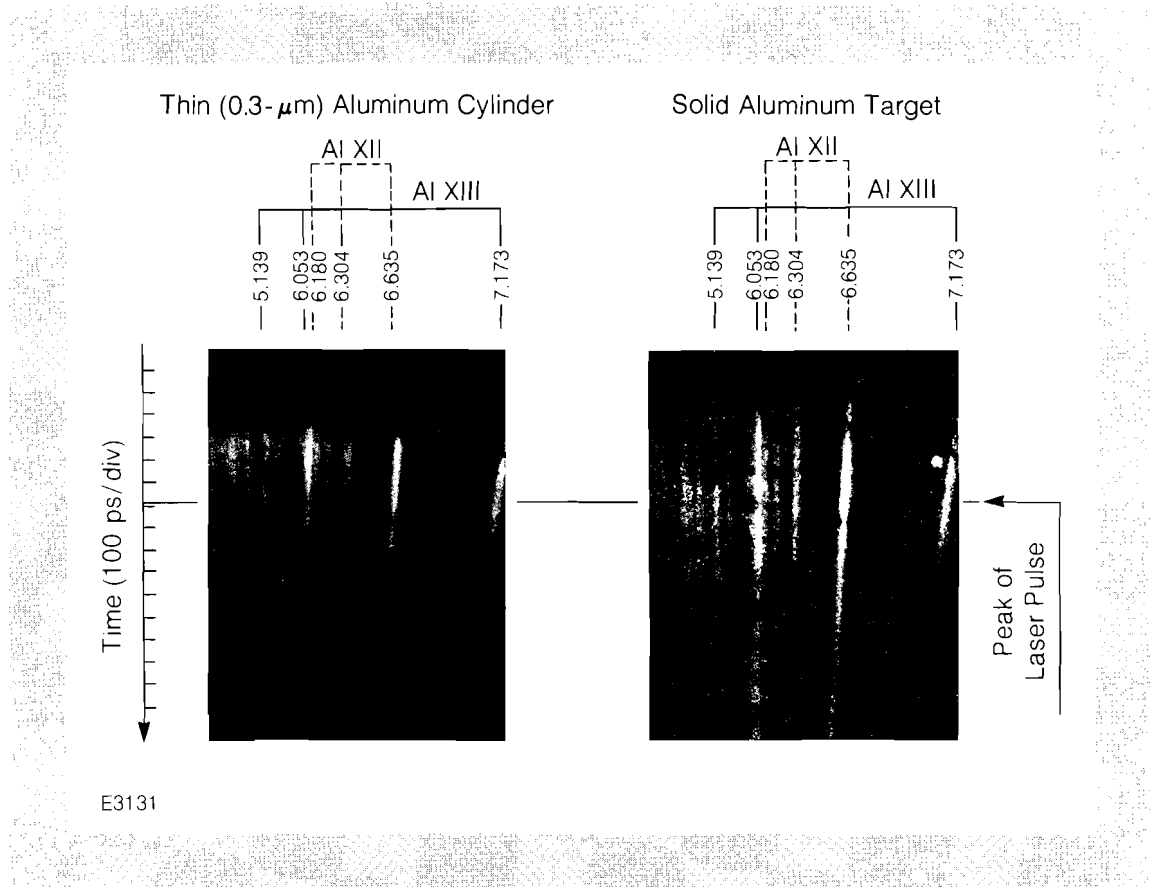
Fig. 21.21
Time-resolved x-ray line spectra recorded from cylindrical targets.

This initial investigation of the plasma created by imploding cylindrical targets has provided some interesting data from which future studies can optimize the production of linear plasmas suitable as x-ray laser media. From the present studies it is clear that thick, ablatively driven cylindrical shells will only implode symmetrically under illumination conditions more uniform than those used in these investigations.

However, the submicron-thick metallic shells, which rapidly decompress on irradiation, implode symmetrically to produce conditions that appear to be similar to those predicted by the 1-D code *LILAC*. Further studies are planned to examine in detail the production of specific levels during shell implosions.

ACKNOWLEDGMENT

REFERENCES

1. For a general review of short-wavelength laser approach, see R. W. Waynant and R. C. Elton, *Proc. IEEE* **64**, 1058 (1976); F. V. Bunlain, V. I. Derzhiev, and S. I. Yakovlenka, *Sov. J. Quantum Elect.* **11**, 981 (1981).

2. M. D. J. Burgess, R. Dragila, B. Luther-Davies, K. A. Nugent, A. J. Perry, G. J. Tallents, M. C. Richardson, and R. S. Craxton (submitted for publication).

3. J. M. Soures, R. J. Hutchison, S. D. Jacobs, L. D. Lund, R. L. McCrory, and M. C. Richardson, in Proceedings of the 10th Annual Meeting of the American Nuclear Society (1983).

4. H. Kim, S. Noyes, and M. C. Richardson, to be presented at the 12th International Conference on Metallurgical Coatings, Los Angeles, CA, 15–19 April 1985.

5. M. C. Richardson, R. S. Marjoribanks, S. A. Letzring, J. M. Forsyth, and D. M. Villeneuve, *IEEE J. Quantum Electr.* **QE-19**, 1861 (1983).

6. P. A. Jaanimagi and B. L. Henke, *Rev. Sci. Instrum.* (to be published).

3.B   Two-Dimensional Electric Field Mapping with Subpicosecond Resolution

Very high-speed semiconductor devices, including the hetero-junction bipolar transistor, GaAs MESFET, TEGFET, and MODFET, have a response well within the picosecond regime; for characterization of these ultrafast devices, new instrumentation is needed. Such instrumentation should have good spatial resolution of a few micrometers, a temporal response of a few picoseconds, and minimum interference with the circuit.

We have demonstrated such a technique, which is based on the electro-optic sampler developed earlier at LLE.[1-3] The new method is capable of characterizing the response of microstructures in two dimensions with a temporal resolution of a fraction of a picosecond.

The geometry of the new reflection-mode sampling is shown in Fig. 21.22. A thin slab of $LiTaO_3$ is located near the surface of a coplanar transmission line built on Cr:GaAs substrate. The electrode widths, as well as the distance between electrodes, are 50 μm. The bottom face of the $LiTaO_3$ is covered with a high-reflection coating. An electrical signal is generated by laser-induced photoconductivity in a gap which interrupts one of the electrodes. The gap is 50-μm wide and biased with a few tens of volts. As the signal propagates down the strip line, its fringing field penetrates into the thin slab of $LiTaO_3$ and slightly modifies the crystal birefringence according to the signal strength. This electrically induced change is detected by a probe beam, which is reflected by the dielectric coating. Presently the spatial resolution is 10–15 μm, which can be improved to 0.5 μm by focusing the beam more tightly. Figure 21.23 shows the experimental results when 100-fs optical pulses are used to generate and probe the electrical pulses. The temporal resolution is 0.75 ps in this experiment. The resolution is limited by the double-pass transit time of the probe pulse across the region of induced birefringence; the depth of this region scales down with the electrode spacing. Thus, the transit-time effect can be reduced and the temporal resolution improved simply by reducing the dimensions of the coplanar strip line. In the near future very high-speed Si- or GaAs-integrated circuits will be tested using this technique.

E2895
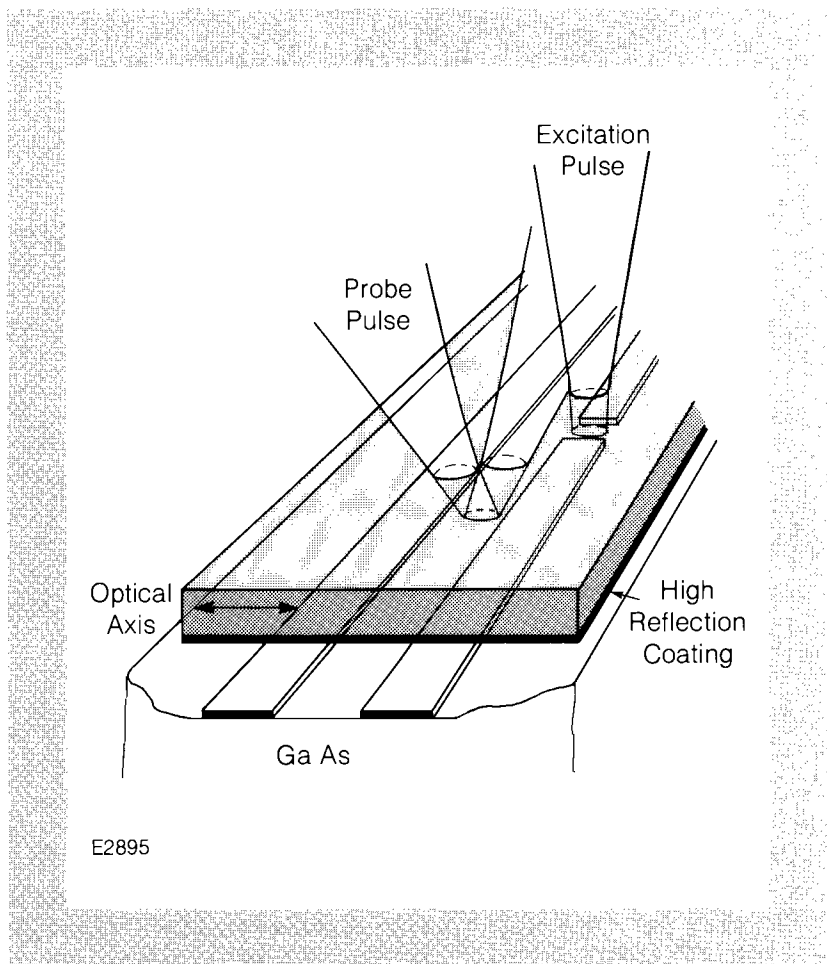
Fig. 21.22
Reflection-mode electro-optic sampler configuration.
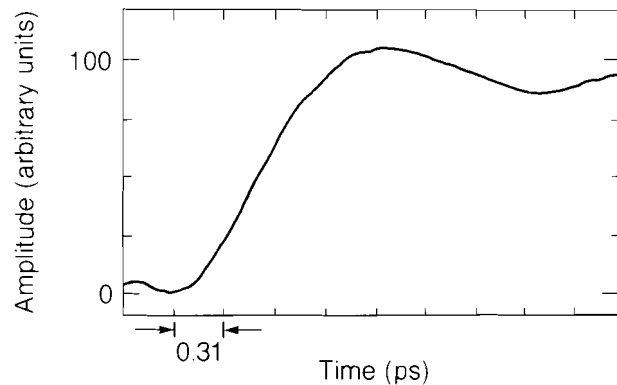
Fig. 21.23
Temporal response of the reflection-mode
sampler with coplanar strip-line dimensions
of 50 μm. The 10–90% rise time is 0.75 ps.

An alternative sampling technique takes advantage of the electro-optic properties inherent in the GaAs. In this mode, the GaAs device being characterized also serves as the sampling medium; this practically eliminates any interference with the device operation. This technique requires a probe pulse with a wavelength greater than 900 nm in order to avoid band-to-band absorption. Short pulses in the IR regime can be obtained by starting with 620-nm pulses created by a synchronously pumped anti-resonant ring laser.[4] The pulses are amplified with a 1-KHz dye amplifier chain and regenerative amplifier;[5] a white-light continuum in a water cell is then generated. This new sampling configuration is currently under investigation.

ACKNOWLEDGMENT

REFERENCES

1. J. A. Valdmanis, G. A. Mourou, and C. W. Gabel, *Appl. Phys. Lett.* **41**, 211 (1982).

2. J. A. Valdmanis, G. A. Mourou, and C. W. Gabel, *IEEE J. Quantum Electron.* **QE-17**, 664 (1983).

3. G. A. Mourou and K. E. Meyer, *Appl. Phys. Lett.* **45**, 492 (1984).

4. T. Norris, T. Sizer, and G. A. Mourou, *J. Opt. Soc. Am. B* (to be published).

5. I. Duling, T. Norris, T. Sizer, P. Bado, and G. A. Mourou, *J. Opt. Soc. Am. B* (to be published).

3.C Kilohertz, Synchronous Amplification of 85-fs Optical Pulses

In recent years significant advances have been made in the generation and amplification of ultrashort optical pulses. The amplification of ultra-short pulses allows high (gigawatt) peak powers to be obtained, making it possible to investigate nonlinear phenomena occurring on the pico-second or femtosecond (fs) time scale. Of particular interest is the generation of the white-light continuum, which is obtained by focusing a laser pulse with intensities in excess of 10^{11} W/cm^2 in a clear liquid such as water or ethylene glycol.[1] The continuum is useful as a source of ultrashort pulses in the spectral range from the near IR to the near UV.

Two general schemes have been reported for providing ultrashort, amplified femtosecond laser pulses. In one method, pulses of duration of the order of 100 fs are generated in a cw-pumped and colliding-pulse mode-locked (CPM) dye laser.[2] The pulses are then amplified to the 100-μJ level by pumping an amplifier chain with nanosecond pulses from a frequency-doubled Q-switched Nd:YAG laser.[3] Since the pump pulses are much longer than the storage time of the dye amplifier medium, there is no severe requirement for synchronization between the oscillator pulses and amplifier pump pulses. In the second method, the subpicosecond pulses are generated in a synchronously pumped, pas-sively mode-locked dye laser,[4] and are amplified by 90-ps pump pulses that are synchronized to the dye laser pulses[5,6] to within about 40 ps. Because the pump pulses are now of duration of the order of the dye storage time, a strict synchronization is required between the oscilla-tor and pump pulses. Only a synchronously pumped oscillator-amplifier configuration is capable of satisfying this condition. The advantages of pumping the amplifier chain synchronously with short (< 100-ps) pump pulses include increased efficiency, stability, and energy contrast between the amplified pulse and amplified spontaneous emission. Both methods are capable of producing peak powers of a few gigawatts at repetition rates of about 10 Hz.

Here we report the development of an oscillator-amplifier system that offers two significant advantages over the systems discussed above. We have developed a dye laser that is both synchronously pumped and colliding-pulse mode locked, making synchronous amplification of a CPM laser possible for the first time.[7] Second, we have developed a cw-pumped regenerative Nd:YAG amplifier that can produce 1-mJ, 100-ps pulses at a repetition rate of 1 kHz. In this oscillator-amplifier system, the CPM dye laser is synchronously pumped by the frequency-doubled output of a cw mode-locked Nd:YAG laser. The Nd:YAG laser is also used to seed the regenerative amplifier. The output of the regenerative amplifier is frequency doubled and is used to pump a two-stage dye amplifier chain. Timing between the oscillator and pump pulses is achieved using an optical delay line. With this system, we have succeeded in amplifying the 85-fs CPM pulses to the microjoule level, sufficient to produce the white-light continuum at a 1-kHz repetition rate. In what follows we discuss in detail the two new amplifiers: the regen-erative Nd:YAG amplifier and the dye amplifier chain.

Nd:YAG Regenerative Amplifier

The pump source for the new dye laser amplifier is the output of a recently developed Nd:YAG regenerative amplifier.[8] In the past the repetition rate of Nd:YAG amplifiers has been limited to about 30 Hz by the flashlamps and power supplies. Alternatively, a cw mode-locked and Q-switched laser could be used as the dye amplifier pump source; however, the selection of a single pulse from the Q-switched pulse train reduces the available energy to about 100 μJ. In addition, the repetition rate of such a system is limited to 500 Hz to ensure good stability. All of these limitations can be overcome by using a cw Nd:YAG operated as a regenerative amplifier.

The configuration of a system in which such an amplifier is integrated as the source for a dye amplifier is shown in Fig. 21.24. The input pulse is a portion of the 1.06-μm radiation from the cw mode-locked Nd:YAG laser that is used to pump the dye laser. These pulses are then injected into a fiber for transport to the regenerative amplifier. The use of a fiber not only decouples the alignment of the two lasers, but also allows the oscillator and amplifier to be in different locations (tables or even rooms) without need for long beam paths. A 4% reflector follows the fiber to isolate the cw mode-locked Nd:YAG from the amplifier. The reflector also serves to protect the fiber from being damaged by leakage from the amplifier. The injected pulses are of approximately 10-pJ energy and 100-ps duration. A quarter-wave plate is placed in the cavity both to frustrate cw lasing and to reject the injected pulses after two round trips. The amplifier is triggered by applying a voltage sufficient for a quarter-wave rotation to the injection Pockels cell (PC 2) to compensate

Fig. 21.24
Synchronous dye amplifier system. The Nd:YAG regenerative amplifier configuration is detailed inside the dotted line. The Nd:YAG amplifier can produce 1-mJ, 100-ps pulses at 1 kHz. The dye amplifier produces 170-fs pulses with energy 1.5 μJ, or 1.7-ps pulses with energy 5 μJ.
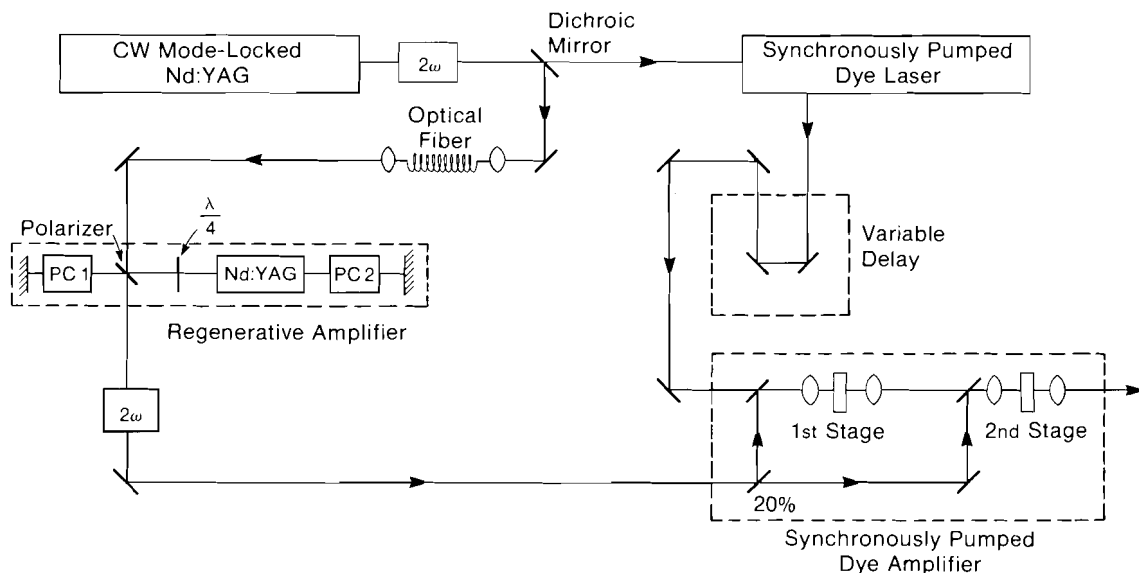
E3126

for the quarter-wave plate. This action not only Q-switches the laser but also traps one of the injected pulses in the cavity. Following approximately 45 round trips (500 ns), the cavity-dumping Pockels cell (PC 1) is triggered and the pulse is rejected from the cavity.

The system can currently be triggered at any repetition rate up to 1.6 kHz, limited by the Pockels cell driver power supply. A plot of output pulse energy versus repetition rate is shown in Fig. 21.25. It is expected that the pulse energy will remain constant until the repetition rate approaches the inverse storage time of the Nd:YAG (5 kHz). This would indicate that the rolloff at 1 kHz present in Fig. 21.25 is due to either uncertainty in the measurement or a thermal effect in the Pockels cells. The output pulse energy is 0.8 mJ in routine operation, although values as high as 1.1 mJ have been obtained at 1 kHz. This limit is due to the high-contrast dielectric polarizer which must be inserted in the cavity.
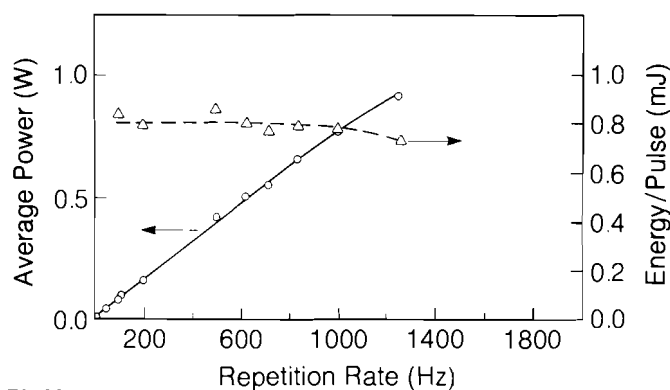
Fig. 21.25
Energy per pulse and average power vs repetition rate for the cw-pumped Nd:YAG regenerative amplifier.

E3160

Since the amplifier is used as a source of pump pulses for the dye amplifiers, the 1.06-μm pulses were frequency doubled using a 3-mm KTP crystal. Energies of 250 μJ at 532 nm are obtained (30% efficiency). Efficiencies as high as 50% have been observed, but this resulted in damage to the KTP crystal. The output energy stability of this system is shown in Fig. 21.26, which is a histogram of the doubled energy output of the Nd:YAG regenerative amplifier. The full width at half maximum of the energy distribution is 2.3%, with 99% of the shots falling within ± 2.7%.

Dye Amplifier

The dye amplifier is configured as a standard two-stage, collinearly pumped amplifier, as shown in Fig. 21.24.[5] The stages are 1 cm in length, with flowing Kiton Red of 4×10^{-5} Molar concentration in water. The spot sizes in the first and second stages are 25 μm and 150 μm, respectively. The first stage is pumped by 20% of the green energy. The input dye laser pulse energy is from the synchronously pumped CPM laser, with a pulse width of 85 fs.[7] After transport to the amplifier, the pulse energy is approximately 350 pJ. After the losses of the unpumped amplifier chain, the transmitted energy is 150 pJ. The

combined gain of the two stages is 10^4, resulting in an output energy of 1.5 μJ.

An autocorrelation of the amplified dye laser pulses is shown in Fig. 21.27. The trace indicates a pulse width of 170 fs, assuming a $sech^2$ pulse shape. The presentation of the autocorrelation trace as points is due to the limitation of our computer-controlled data acquisition and
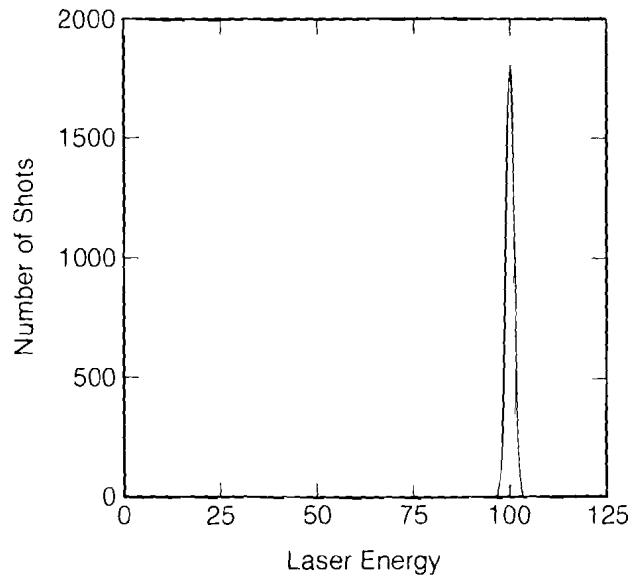
E3163

Fig. 21.26
Histogram of the energy of the frequency-doubled output of the Nd:YAG regenerative amplifier. Ninety-nine percent of the pulses lie within ± 2.7%.
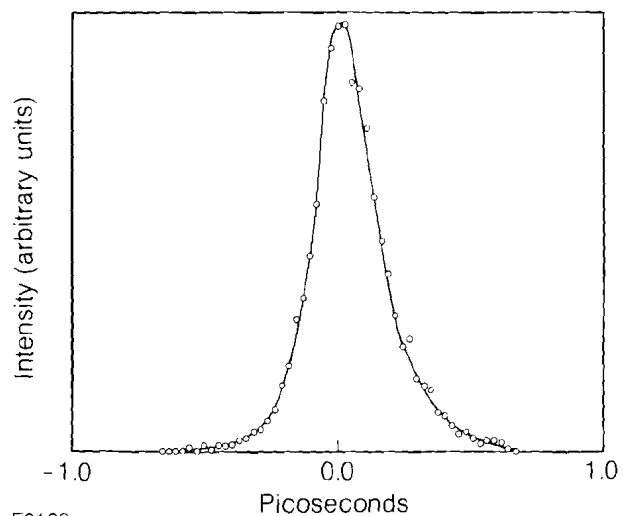
E3162

Fig. 21.27
Autocorrelation of the amplified dye pulses. For an input pulse width of 85 fs, the output pulse width was 170 fs, assuming a $sech^2$ pulse shape. No saturable absorber or grating pair was used to limit the pulse broadening.

not caused by the repetition rate of the laser. Some form of gating of the collection scheme is required in order to remove the background signal from the cw dye laser output. Broadening of the pulse is caused by both dispersion in the amplifier chain as well as saturation of the gain. The unamplified beam, if allowed to propagate through the amplifier chain, shows broadening due to dispersion to approximately 120 fs, which presumably could be removed with a grating pair. The remaining broadening is due to gain saturation. This was confirmed by observing that the amplified pulse width became 120 fs if the dye input energy was reduced significantly. No saturable absorbers or negatively dispersive elements were used to reduce the output pulse width.

It was found that the white-light continuum could be generated in water with as little as 250 nJ when a 7x objective was used for focusing. This low threshold indicates that the beam quality (focusability) of the amplified pulses is very good, as is expected from a longitudinally pumped amplifier.

When the saturable absorber jet in the dye laser was removed so the pulse width was 1.7 ps and the laser was tuned to the peak of the Kiton Red gain, the output energy increased to 5 μJ. It is interesting to note that when the spectrum of the amplified pulse and ASE were examined, the ASE energy decreased by a factor of 3 when the dye laser was being amplified compared to when the dye laser was blocked. This would indicate that all energy measurements are underestimated if the ASE is determined by blocking the dye laser input.

Conclusion

Development of a kHz Nd:YAG regenerative amplifier and a synchronously pumped CPM dye laser has enabled the high-repetition-rate amplification of ultrashort optical pulses to the microjoule level. The pulse width broadens from 90 fs to 180 fs due to gain saturation and dispersion in the amplifier chain.

Two improvements to the system are planned in the near future. First, a saturable absorber will be inserted between the two dye amplifier stages to suppress the ASE and to control the preferential amplification of the leading edge of the pulse due to gain saturation. Second, temporal broadening due to dispersion will be removed by use of a dispersive delay line consisting of a grating pair. With these additions, the amplifier should produce megawatt pulses shorter than 100 fs at kHz repetition rates.

ACKNOWLEDGMENT

REFERENCES

1. R. L. Fork et al., Opt. Lett. **8**, 1 (1983).

2. R. L. Fork, B. I. Greene, and C. V. Shank, Appl. Phys. Lett. **38**, 671 (1981).

3. R. L. Fork, C. V. Shank, and R. T. Yen, *Appl. Phys. Lett.* **41**, 223 (1982).

4. G. A. Mourou and T. Sizer II, *Opt. Commun.* **41**, 47 (1982).

5. T. Sizer II, J. D. Kafka, A. Krisiloff, and G. A. Mourou, *Opt. Commun.* **39**, 259 (1981).

6. T. Sizer II, J. D. Kafka, I. N. Duling III, C. W. Gabel, and G. A. Mourou, *IEEE J. Quantum Electron.* **QE-19**, 506 (1983).

7. T. Norris, T. Sizer II, and G. A. Mourou, to be published in *J. Opt. Soc. Am. B, Special Issue on Femtosecond Optical Interactions.*

8. I. N. Duling, P. Bado, S. Williamson, G. Mourou, and T. Baer, presented at the Conference on Lasers and Electro-Optics, Anaheim, CA, paper PD3 (1984).

Section 4
NATIONAL LASER USERS
FACILITY NEWS

This report covers the activities of the National Laser Users Facility during the quarter 1 October to 31 December 1984. Scientists from six different user experiments visited LLE during this period; three continued experiments on the facility. **Humberto Figueroa** (UCLA); **Alan Hauer** (Los Alamos); **Burton Henke** (University of Hawaii); **C. F. Hooper, Jr.** (University of Florida); **John Seely, Charles M. Brown,** and **W. E. Behring** (Naval Research Laboratory); and **George Miley** (University of Illinois) visited LLE to discuss past or current user experiments.

The following investigators continued current experiments. **Uri Feldman** (Naval Research Laboratory) and co-investigators **John Seeley, Charles M. Brown,** and **W. E. Behring** have been examining the XUV spectra of various high-Z elements that are relevant to x-ray laser research. **C.F. Hooper, Jr.** (University of Florida) has begun to study the implosion dynamics of the fuel by examining the x-ray spectra of gas-filled targets. **Burton Henke** (University of Hawaii) and co-investigator **Paul Jaanimagi** have utilized a time-resolving x-ray spectrograph to study thermal transport. **Burton Henke** is the originator of the diagnostic; **Paul Jaanimagi** is the principal researcher on the experiment.

This experiment by the University of Hawaii provides a very powerful research tool for diagnosing the transient nature of laser-produced plasmas. This diagnostic has been implemented on the OMEGA laser system and is currently in use at LLE.

The diagnostic, the SPEAXS (streak-photographic-elliptic-analyzer x-ray spectrograph) system[1] (see Fig. 21.28), consists of two identical x-ray crystal spectrographs. A time-integrating channel (recorded on photographic film) provides absolutely calibrated x-ray spectra. The spectra from the second channel is time resolved with an x-ray streak camera. The spectral range from 100 to 10,000 eV can be diagnosed by using different 2-D-spacing analyzer crystals. The instrument has been calibrated and tested at the University of Hawaii and has been an on-line diagnostic on the OMEGA facility. A summary of their recent experimental data is presented below.
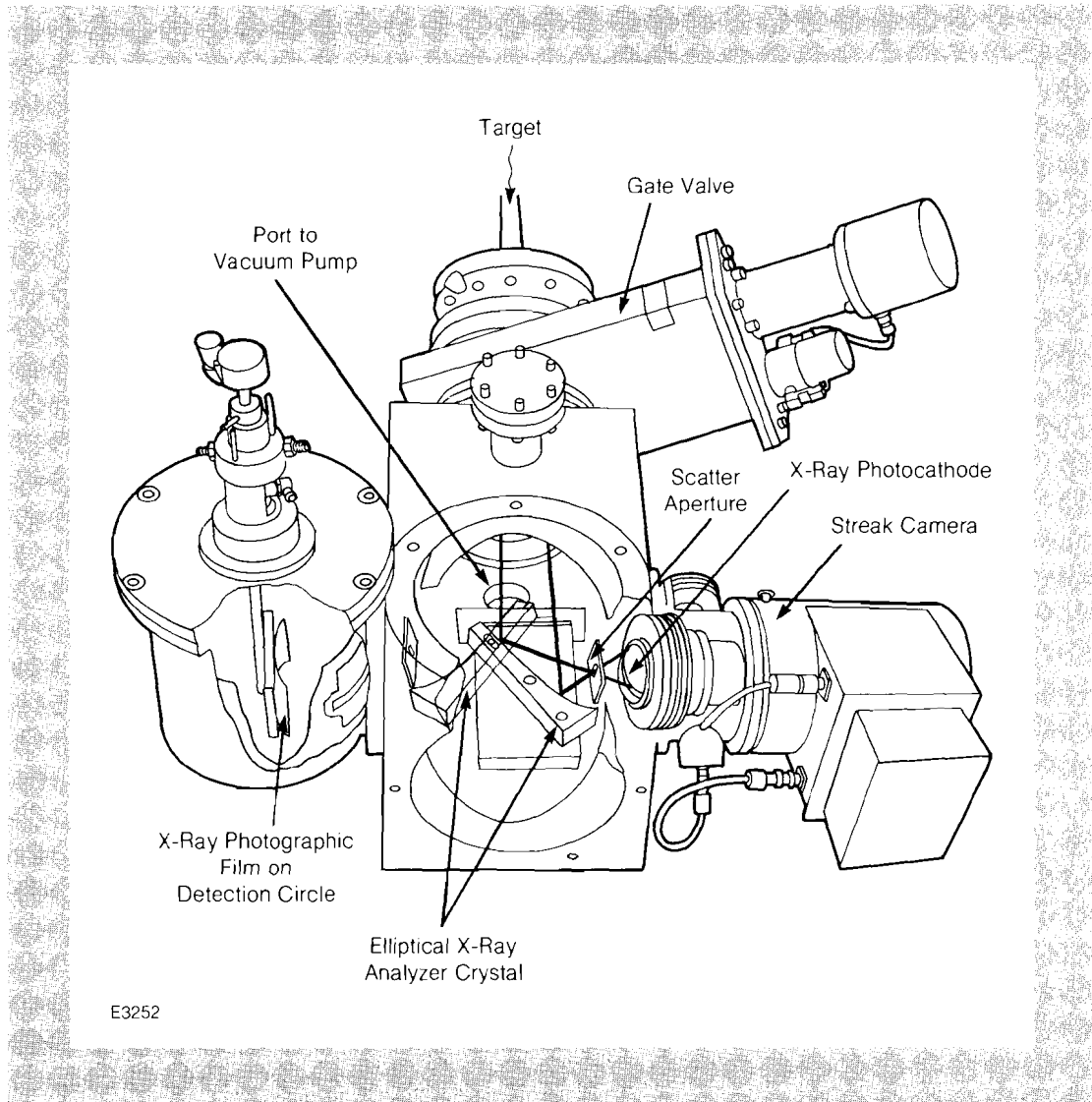
Fig. 21.28
Schematic of the twin-channel, streak-photographic-elliptic-analyzer x-ray spectrograph (SPEAXS system).

The SPEAXS system has been used extensively in the 6- and 12-beam UV-laser campaigns on OMEGA. The main experimental program for this diagnostic has been to study thermal transport. The SPEAXS system has contributed valuable time-resolved data to the high-Z, Au experiments in cooperation with LANL and also to LLE's x-ray laser program.

The thermal transport experiments were performed predominantly with six UV beams. Time-resolved x-ray spectroscopic measurements were made of the progress of the ablation surface through thin layers of material on the surface of the targets. Aluminum layers of various thicknesses on thin- and thick-wall, glass-shell targets were used. Also, the burn-through of CH layers on thin-wall, glass-shell targets was studied. These latter targets were overcoated with a 150-Å Au layer in order to provide a timing fiducial. An example of the time-resolved data is shown in Fig. 21.29. Data on the mass ablated from the Au/CH/glass
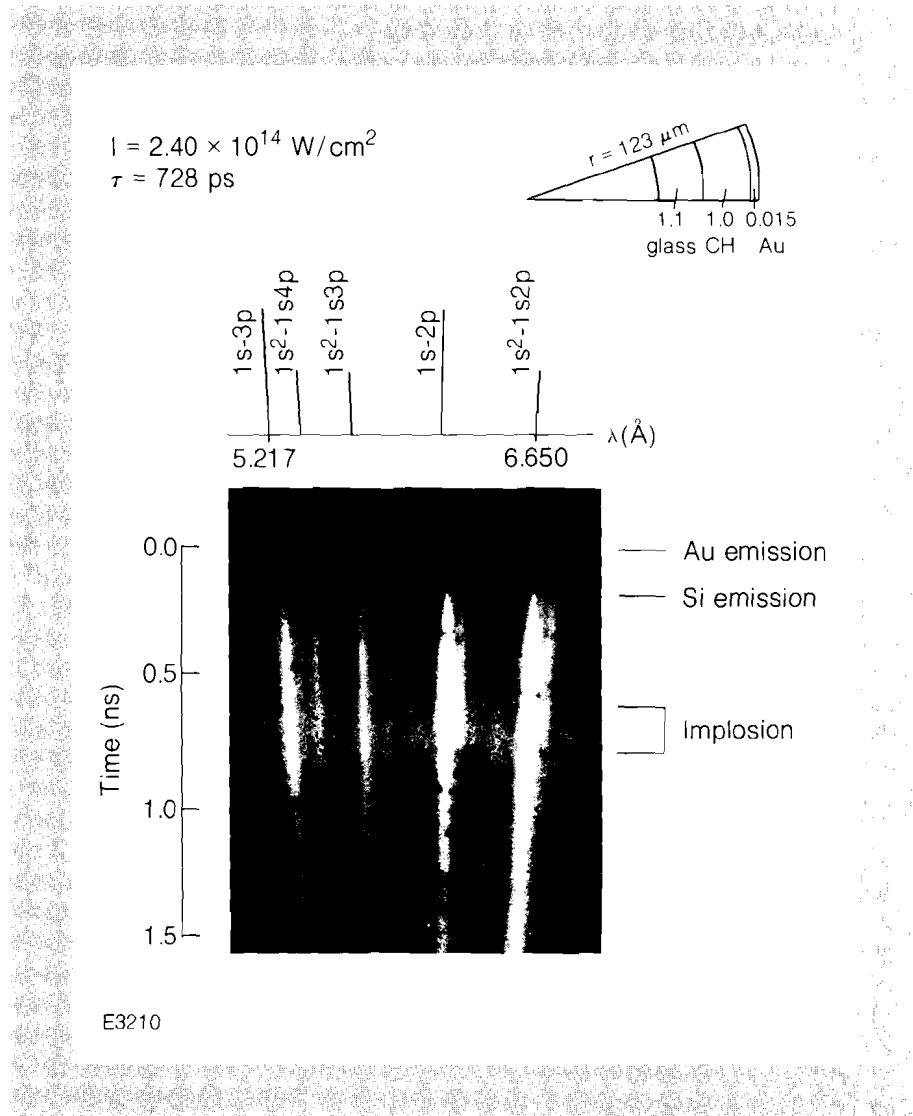
Fig. 21.29
Time-resolved x-ray spectrum from an Au/CH/glass target using a PET analyzer crystal.

targets are presented in Fig. 21.30. The experimental points on this plot use the mass of Au layer ($\sim$ 45 ng) or the mass of the Au+CH layers (200–800 ng) of the targets. The gold layer is assumed to have been ablated by the time we observe its x-ray emission. Similarly, the onset of the silicon line emission denotes the burn-through time for the CH layer. The absorbed energy is derived from the time-dependent absorption as predicted by LILAC simulations. Since we are observing x-ray emission in the 1.7- to 2.5-keV range, we consider the 500-eV isotherm
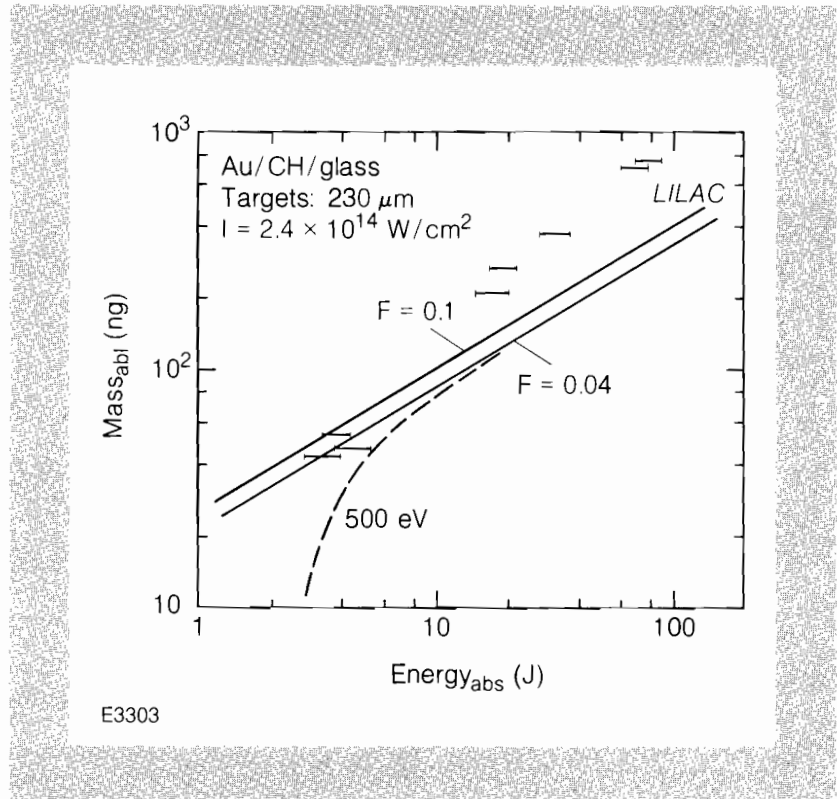
Fig. 21.30
Fig. 21.30
Mass-ablated versus absorbed energy during a target shot for Au/CH/glass-shell targets, ~230 μm in diameter at I = 2.4×10^{14} W/cm². Comparison with LILAC code simulations with flux limiters of F = 0.04 and 0.1.

as the mass-ablation surface for comparisons with code predictions. The qualitative agreement of the absorbed energy dependence for the ablated mass is good but quantitative agreement is poor.

The mass-ablation rate for CH burn-through, as derived from the time-resolved data, is in good agreement with time-integrated data,[2] as presented in Fig. 21.31. The discrepancy in the mass-ablation rate between experiments and *LILAC* code simulations is ascribed to nonuniform irradiation with only six UV beams.[3] The presence of hot spots in any of the incident laser beams will dominate the burn-through of the CH layer and result in too large a value for the mass-ablation rate.

Preliminary results (two target shots) with 12 UV beams support the nonuniformity argument. The experimentally measured, mass-ablation rate with 12-beam irradiation is in much closer agreement with *LILAC* code simulations.

During FY84 (1 October 1983 to 30 September 1984), the user program accumulated a total of 259 target shots on both the GDL and the OMEGA facilities. Table 21.III summarizes the total number of target shots by users. Additional information on these experiments can be obtained from the appropriate investigators.

On 4 March 1985, the National Laser Users Facility Steering Committee will hold its sixth meeting. The committee meets to review and approve proposals and to recommend funding of approved proposals in inertial fusion to the U. S. Department of Energy. This funding allocation is separate from LLE's operation agreement and is
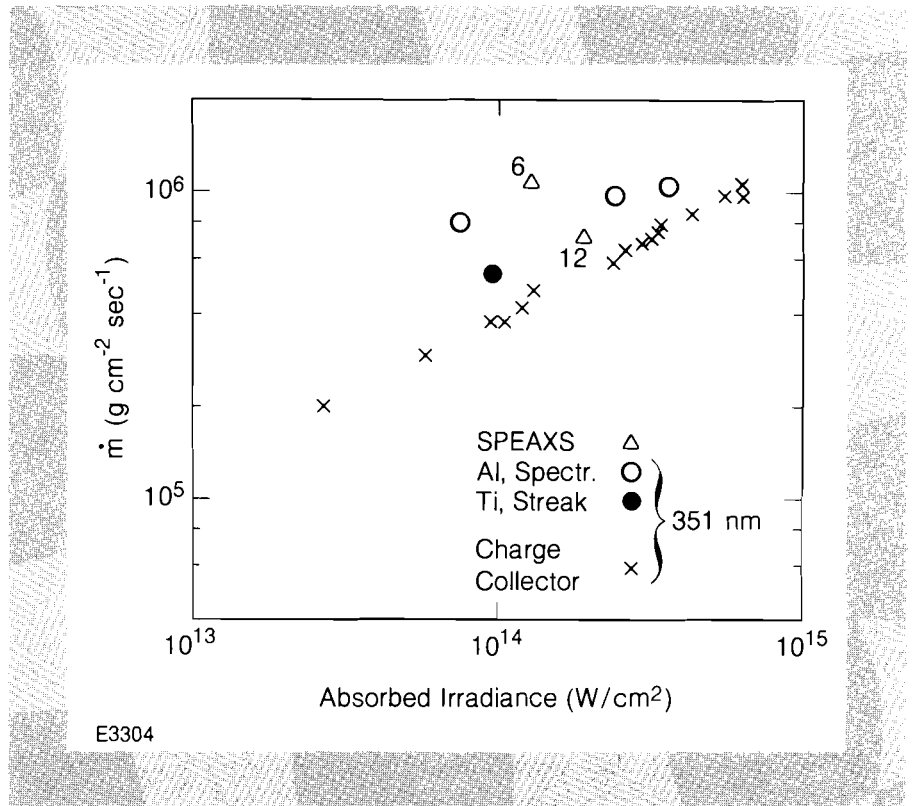
Fig. 21.31
Mass-ablation rate in spherical geometry, six-beam UV-laser irradiation; one point with 12-beam laser.

designed to provide research funds to users in the inertial fusion and related scientific areas. Users in other fields may use the facility but must provide their own research funds.

The committee consists of

User (Affiliation)	Experiment	Number of Shots	
		GDL	OMEGA
J. Kent Blasie and Leo Herbette (U. of Pennsylvania and U. of Connecticut)	Biophysics	38	—
Phil Burkhalter (Naval Research Laboratory)	X-Ray Laser	—	33
Ray Elton (Naval Research Laboratory)	X-Ray Laser	7	—
Uri Feldman (Naval Research Laboratory)	XUV Spectroscopy	—	35
Hans Griem (U. of Maryland)	Plasma Physics	—	26
Burton Henke and Paul Jaanimagi (U. of Hawaii)	X-Ray Diagnostics	—	67
Chan Joshi and Nizar Ebrahim (UCLA and Yale University)	Plasma Physics	52	—
		98	161
		TOTAL	259

U96

Table 21.III
Summary of user shots for FY84.

Last year, 21 proposals were submitted; ten were approved. The next issue of the LLE Review will list the new approved proposals.

The users guide has been revised to include a description of the OMEGA and GDL experimental facilities and information for the preparation of user proposals. Copies of this revised guide and any further information on the National Laser Users Facility are available from:

Thomas C. Bristow, Manager
National Laser Users Facility
Laboratory for Laser Energetics
University of Rochester
250 East River Road
Rochester, New York 14623-1299
(716) 275-2074

ACKNOWLEDGMENT

REFERENCES

1. B. L. Henke, H. T. Yamada, and T. J. Tanaka, *Rev. Sci. Instrum.* **54**, 1311 (1983); B. L. Henke and P. A. Jaanimagi, submitted to the *Review of Scientific Instruments*.

2. LLE Review **17**, 32 (1983).

3. LLE Review **20**, 150 (1983)

PUBLICATIONS AND CONFERENCE PRESENTATIONS

Publications

G. A. Mourou and K. E. Meyer, "Subpicosecond Electro-Optic Sampling Using Coplanar Strip Transmission Lines," *Appl. Phys. Lett.* **45**, 492–494 (1984).

J. M Soures, review of *The High-Power Iodine Laser* by G. Brederlow, E. Fill, and K. J. Witte, *IEEE J. Quantum Electron.* **20**, 1098 (1984).

S. Kacenjar, L. M. Goldman, A. Entenberg, and S. Skupsky, "$<\rho R>$ Measurements in Laser-Produced Implosions Using Elastically Scattered Ions," *J. Appl. Phys.* **56**, 2027–2032 (1984).

J. P. Matte, T. W. Johnston, J. Delettrez, and R. L. McCrory, "Electron Heat Flow with Inverse Bremsstrahlung and Ion Motion," *Phys. Rev. Lett.* **53**, 1461–1464 (1984).

R. L. Keck, L. M. Goldman, M. C. Richardson, W. Seka, and K. Tanaka, "Observations of High-Energy Electron Distributions in Laser Plasmas," *Phys. Fluids* **27**, 2762–2766 (1984).

C. J. McKinstrie, A. Simon, and E. A. Williams, "Nonlinear Saturation of Stimulated Raman Scattering in an Homogeneous Plasma," *Phys. Fluids* **27**, 2738–2743 (1984).

M. Strauss, G. Hazak, D. Shvarts, and R. S. Craxton, "Magnetic Field Effects on Electron Heat Transport in Laser-Produced Plasmas," *Phys. Rev. A* **30**, 2627–2637 (1984).

B. Yaakobi, "X-Ray Lithography Using Laser Plasma as a Source," *Solid State Technology* **11**, 239–240 (1984).

A. Simon and R. W. Short, "New Model of Raman Spectra in Laser-Produced Plasma," *Phys. Rev. Lett.* **53**, 1912–1914 (1984).

A. Schmid, D. Smith, M. Guardalben, and J. Abate, "Photothermal-Deflection Analysis of UV Optical Thin Films," *SPIE Vol. 476 — Excimer Lasers, Their Applications, and New Frontiers in Lasers*, edited by Ronald W. Waynant (1984), pp. 136–142.

H. L. Helfer, R. L. McCrory, and H. M. Van Horn, "Further Monte Carlo Calculations for the Classical One-Component Plasma in the Range $100 \leq \Gamma \leq 160$: The FCC Lattice," *J. Stat. Phys.* **37**, 577–588 (1984).

K. Tanaka, L. M. Goldman, W. Seka, R. W. Short, and E. A. Williams, "Spectroscopic Study of Scattered Light at around the Fundamental Wavelength in UV Laser-Produced Plasmas," *Phys. Fluids* **27**, 2960–2965 (1984).

I. N. Duling III, and M. G. Raymer, "Time-Dependent Semiclassical Theory of Gain-Coupled Distributed Feedback Lasers," *IEEE J. Quantum Electron.* **20**, 1202–1207 (1984).

Forthcoming Publications

R. D. Frankel and J. M. Forsyth, "Time-Resolved X-Ray Diffraction Study of Photostimulated Purple Membrane," accepted for publication in *Biophysical Journal*.

I. N. Duling III, T. Norris, T. Sizer II, P. Bado, and G. Mourou, "Kilohertz Synchronous Amplification of 85-fs Optical Pulses," accepted for publication in the *Journal of the Optical Society of America*.

T. Norris, T. Sizer II, and G. Mourou, "Generation of 85-fs Pulses by Synchronous Pumping of a CPM Dye Laser," accepted for publication in the *Journal of the Optical Society of America*.

B. Yaakobi, O. Barnouin, J. Delettrez, L. M. Goldman, R. Marjoribanks, R. L. McCrory, M. C. Richardson, and J. M. Soures, "Thermal Transport Measurements in Six-Beam, UV Irradiation of Spherical Targets," accepted for publication in the *Journal of Applied Physics*.

B. A. Brinker, "Microradiographic Self-Imaging of DT-Filled Inertial Fusion Targets," accepted for publication in the *Journal of Vacuum Science and Technology*.

Conference Presentations

S. D. Jacobs, K. A. Cerqua, T. J. Kessler, and W. Seka, "Retrofit of a High-Power Nd:Glass Laser System with Liquid Crystal Polarizers," presented at the 16th Annual Symposium on Optical Materials for High Power Lasers, Boulder, CO, October 1984.

The following presentations were made at the Twenty-Sixth Annual Meeting of the Division of Plasma Physics of the American Physical Society, Boston, MA, October 1984:

W. Beich, M. Dunn, R. Hutchison, W. Lampeter, T. Kessler, M. C. Richardson, W. Seka, S. Skupsky, J. Soures, and S. Tommer, "Irradiation Uniformity of Spherical Targets by Multiple UV Beams from OMEGA."

T. Boehly, L. M. Goldman, W. Seka, and R. S. Craxton, "Hydrodynamic Efficiency and Thermal Transport in Planar Target Experiments at LLE."

B. Boswell, T. Boehly, J. Delettrez, L. M. Goldman, M. C. Richardson, and S. Sarraf, "Ion Velocity Distributions from Spherical 1054-nm and 351-nm Laser Plasmas."

R. S. Craxton, "Hydrodynamics of Long-Scale-Length Plasmas" (invited).

J. Delettrez, R. Epstein, M. C. Richardson, C. P. Verdon, and B. Yaakobi, "Simulation of Experiments in Spherical Irradiation at λ = 350 nm."

R. Epstein, S. Skupsky, and B. Yaakobi, "Absorption Spectroscopy as a Density Diagnostic for Dense Imploded Shells."

L. M. Goldman, R. Bahr, R. Boni, R. L. McCrory, M. C. Richardson, W. Seka, R. W. Short, and K. Tanaka, "Coronal Spectroscopy in Laser Plasmas."

P. A. Jaanimaagi and B. L. Henke, "Time-Resolved X-Ray Line Emission Studies of Thermal Transport in Multiple-Beam UV-Irradiated Targets."

R. L. Keck, M. C. Richardson, J. M. Soures, and J. Delettrez, "Absorption and Hot Electron Generation in UV (351 nm) Driven Spherical Imploding Targets."

S. A. Letzring, M. C. Richardson, P. D. Goldstone, G. Gregory, and G. Eden, "Coronal Conditions in High-Z Spherical Targets Irradiated by Multibeam 351-nm Radiation."

C. J. McKinstrie and A. Simon, "Nonlinear Saturation of Stimulated Raman Scattering in Collisional Homogenous Plasma."

M. C. Richardson, J. Delettrez, R. L. McCrory, J. M. Soures, C. Verdon, and B. Yaakobi, "Scaling of UV (351-nm) Fusion Implosions Driven by Multiple Beams."

W. Seka, L. M. Goldman, K. Tanaka, B. Boswell, R. Boni, and R. Bahr, "Characteristics of High Energy Laser Matter Interaction Studies."

R. W. Short, "Spatial Structure of Heat Flow Instabilities in Laser Plasmas."

A. Simon and R. W. Short, "Interpretation of Raman Spectra as Enhanced Incoherent Ordinary Scattering."

S. Skupsky, R. L. McCrory, and C. P. Verdon, "To What Extent Will Small-Scale Laser-Beam Fluctuations 'Seed' the Rayleigh-Taylor Instability in Direct-drive Targets?"

J. M. Soures, R. Hutchison, S. Jacobs, R. L. McCrory, R. Peck, M. C. Richardson, and W. Seka, "Operational Characteristics of the OMEGA Short-Wavelength Laser Fusion Facility."

K. Swartz and R. W. Short, "Heat Transport by Non-Maxwellian Electrons."

K. Tanaka, B. Boswell, R. S. Craxton, L. M. Boldman, W. Seka, R. W. Short, J. M. Soures, R. Bahr, and F. Guglielmi, "Parametric Processes in Underdense UV Laser-Produced Plasmas."

B. Yaakobi, O. Barnouin, J. Delettrez, R. L. McCrory, M. C. Richardson, and J. M. Soures, "Transport Measurements on Targets Imploded by 12 UV Beams of OMEGA."

P. D. Goldstone, R. H. Day, G. Eden, F. Ameduri, W. C. Mead, S. R. Goldman, M. C. Richardson, R. L. Keck, W. Seka, G. Pien, J. M. Soures, R. L. McCrory, and J. Knauer, "Interaction Physics and X-Ray Emission in High-Z Plasmas at 351 nm."

R. S. Marjoribanks, G. Stradling, M. C. Richardson, A. Hauer, O. Barnouin, B. Yaakobi, S. A. Letzring, and P. D. Goldstone, "Spectral and Temporal Characteristics of X-Rays from Spherical High-Z Targets Irradiated with 351-nm Laser Light."

S. A. Letzring, M. C. Richardson, P. C. Goldstone, G. Gregory, and G. Eden, "Coronal Conditions in High-Z Spherical Targets Irradiated by Multibeam 351-nm Radiation."

S. R. Goldman, W. C. Mead, P. D. Goldstone, and M. C. Richardson, "Energy Penetration and Profile Steepening in High-Z Plasmas."

The following presentations were made at the Annual Meeting of the Optical Society of America, San Diego, CA, October 1984:

I. N. Duling III, T. Norris, T. Sizer II, P. Bado, and G. Mourou, "Synchronous Amplification of Optical Pulses at Kilohertz Repetition Rates."

S. D. Jacobs, K. A. Cerqua, H. Kim, and J. F. Mason, "Polymeric Liquid-Crystal Laser-Blocking Filters."

S. D. Jacobs, A. L. Hrycin, and C. Baldwin, "Dynamically Loaded Scratch Tester for Thin Film Adhesion Measurements."

G. Mourou and S. Williamson, "Time-Resolved Laser-Induced Phase Transformation in Aluminum," presented at the meeting of the Materials Research Society, Boston, MA, November 1984.

The following presentations were made at the American Vacuum Society Symposium, Reno, NE, December 1984:

B. A. Brinker, "Microradiographic Self-Imaging of DT-Filled Inertial Fusion Targets."

F. Guglielmi, "Fabrication of Polymeric Microballoons for Ablative Inertial Fusion Targets," and "Low Density Foam for Self-Focusing Inertial Fusion Targets."

H. Kim, "X-Ray Microradiography of Inertial Fusion Target Using the Laser-Produced Plasma as an X-Ray Source."

S. Noyes and H. Kim, "Aluminum/Aluminum Nitride Sputter Deposition on the Inertial Fusion Target Using the Pulsed Gas Process."